

Czech Technical University in Prague
Faculty of Nuclear Sciences and Physical
Engineering

Department of Physical Electronics
Photonics

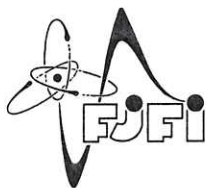


Ultrasensitive nanoscopy with phase detection

Ultracitlivá nanoskopie s fázovou detekcí

MASTER THESIS

Author: Bc. Kateřina Jiříková
Supervisor: Mgr. Marek Piliarik, Ph.D.
Academic year: 2023/24



ČESKÉ VYSOKÉ UČENÍ TECHNICKÉ V PRAZE
FAKULTA JADERNÁ A FYZIKÁLNĚ INŽENÝRSKÁ
Katedra fyzikální elektroniky

ZADÁNÍ DIPLOMOVÉ PRÁCE

<i>Student:</i>	Bc. Kateřina Jiříková
<i>Studijní program:</i>	Fyzikální elektronika
<i>Specializace:</i>	Fotonika
<i>Akademický rok:</i>	2022/2023
<i>Název práce:</i> (česky)	Ultracitlivá nanoskopie s fázovou detekcí
<i>Název práce:</i> (anglicky)	Ultrasensitive nanoscopy with phase detection
<i>Jazyk práce:</i>	Angličtina

Cíl práce:

Cílem diplomové práce bude využití technologie ultracitlivé fázové detekce v interferenční mikroskopii rozptýleného světla extrémně malých objektů a prozkoumání přínosu měření fáze pro kvantitativní detekci rozptylu. K tomu bude využita interferenční mikroskopie rozptýleného světla (iSCAT) [1,2] doplněná o přesnou kvantitativní detekci fáze rozptýleného světla [3,4]. Studentka se zaměří na srovnání detekce fáze a amplitudy rozptylu nanoskopických vzorků (nanočástic, DNA origami konstruktů, nebo proteinů) v prostředí, které různým způsobem ovlivňuje fázi rozptýleného světla – např. opticky homogenní rozhraní, slabě rozptylující povrchy nebo komplexnější vzorky s výrazným interferenčním signálem. V rámci diplomové práce tak bude potvrzena nebo vyvrácena hypotéza vycházející z teoretického modelu fázové neurčitosti rozptylu v důsledku interakce detekovaného dipólového momentu s náhodnou strukturou povrchu v blízkém poli [5,6].

Pokyny pro vypracování:

1. V rešeršní části sesbírejte literaturu věnující se interferenční mikroskopii rozptýleného světla a hmotnostní fotometrii a aplikacím využívajícím detekci fáze ať už pro trasování 3D pohybu nanočástic nebo zachycení prostorové geometrie vzorku. Doplňte ji o srovnání dosažených detekčních limitů a diskusi fundamentálních principů, které tyto detekční limity omezují.
2. V experimentální části využijte fázovou detekci pomocí iSCAT mikroskopie ke statistickému srovnání amplitudy a fáze rozptylu na souboru nanočástic a single-molekulových vzorků v různých prostředích, jako jsou atomárně hladké nebo opticky sladěné

polymerní vrstvy. Diskutujte zdroje neurčitosti detekované fáze v kontextu fyzikálního modelu.

3. Pokuste se navrhnout a ve spolupráci s kolegy ve výzkumném týmu implementovat alternativní přístupy kvantitativní detekce fáze nevyžadující časové skenování aktivním prostorovým modulátorem.

Doporučená literatura:

1. Priest L., Peters J. S., Kukura P., Scattering-based Light Microscopy: From Metal Nanoparticles to Single Proteins, Chemical Reviews 121, 11937, 2021.
2. Piliarik M., Sandoghdar V., Direct optical sensing of single unlabeled proteins and super-resolution imaging of their binding sites, Nature Communications 5, 4495, 2014.
3. Robert H. M. L., Bujak L., Holanová K., Vala M., Henrichs V., Lánský Z., Piliarik M., Fast photothermal spatial light modulation for quantitative phase imaging at the nanoscale, Nature Communications 12, 2921, 2021.
4. Robert H. M. L., Čičala M., Piliarik M., Shaping of Optical Wavefronts Using Light-Patterned Photothermal Metamaterial, Advanced Optical Materials, 2200960, 2022.
5. He Y., S. Lin, H. Robert, H. Li, P. Zhang, M. Piliarik, X.-W. Chen, Multiscale Modeling and Analysis for High-fidelity Interferometric Scattering Microscopy, Journal of Physics D: Applied Physics, 54, 274002, 2021.
6. S. Lin, Y. He, M. Piliarik, X.-W. Chen, Optical Fingerprint of Flat Substrate Surface and Marker-free Lateral Displacement Detection with Angstrom-level Precision, Preprint, arXiv:2208.09772 (to appear in Physical Review Letters).

Jméno a pracoviště vedoucího práce:

Mgr. Marek Piliarik, Ph.D.

Ústav fotoniky a elektroniky AV ČR, v.v.i.

Jméno a pracoviště konzultanta:

doc. Dr. Ing. Ivan Richter

Katedry fyzikální elektroniky, Fakulta jaderná a fyzikálně inženýrská ČVUT v Praze

Datum zadání: 13. říjen 2022

Datum odevzdání: 3. květen 2023

Doba platnosti zadání je dva roky od data zadání.

Richter Ivan

Garant oboru

Richter Ivan

Vedoucí katedry

V. L.

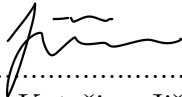
Děkan

V Praze dne 13.10.2022



I hereby declare that I have done this research assignment independently and have used only the materials listed in this work.

Prague, 8th January 2024


.....
Bc. Kateřina Jiříková

Acknowledgements

First of all I would like to thank my supervisor Marek Piliarik for his guidance and constant enthusiasm and motivation for research. I would also like to thank Hadrien M. L. Robert and Yevhenii Shaidiuk for helping me with the experimental part. My thanks also go to the whole Nanooptics team, especially Lucka for her great support and Kristyna for her valuable advice on practical matters. Last but not least, I would like to thank my family and Honza for their support during my studies.

Bc. Kateřina Jiříková

Název práce:

Ultracitlivá nanoskopie s fázovou detekcí

Autor: Bc. Kateřina Jiříková

Studijní program: Aplikace přírodních věd

Obor: Fotonika

Druh práce: Diplomová práce

Vedoucí práce: Mgr. Marek Piliarik, Ph.D.

Ústav fotoniky a elektroniky AV ČR, v.v.i.

Konzultant: Prof. Ing. Ivan Richter, Dr

Katedra Fyzikální Elektroniky, Fakulta Jaderná a
Fyzikálně Inženýrská, ČVUT v Praze

Abstrakt:

V posledních letech došlo v oblasti ultracitlivé mikroskopie k významnému pokroku v citlivosti a kvantitativní povaze měření. Zejména pro pochopení vnitřních struktur opticky tenkých objektů, jako jsou buňky a tkáně, se fázová citlivost stává klíčovou. Tato práce zkoumá nové funkce a implementace v interferometrické rozptylové mikroskopii (iSCAT), která je proslulá svými neinvazivními zobrazovacími schopnostmi bez použití značek. iSCAT je díky své citlivosti na změny fáze ideální metodou pro ultracitlivou detekci fáze, což je klíčový aspekt při pozorování dynamiky jednotlivých molekul. Tato studie demonstruje, jak iSCAT dokáže kvantitativně detekovat fázi rozptýleného světla nezávisle na jeho amplitudě, s cílem zvýšit přesnost kvantifikace makromolekulárních interakcí. Výzkum dále zkoumá, jak fáze ovlivňuje iSCAT kontrast, a ukazuje, že i subnanometrové nerovnosti krycích sklíček mohou významně ovlivnit výsledný interferogram. Tato zjištění nejen zdůrazňují potenciál iSCATu v molekulární biologii, ale také poukazují na nutnost přesnosti v mikroskopickém prostředí, což otevírá cestu k přesnějším a spolehlivějším mikroskopickým analýzám.

Klíčová slova: rozptyl světla, iSCAT, ultracitlivá detekce fáze, zobrazení jednotlivých molekul, fototermální modulátor světla

Title:

Ultrasensitive nanoscopy with phase detection

Author: Bc. Kateřina Jiříková

Course of study: Physical electronics

Field of study: Photonics

Type of thesis: Master Thesis

Advisor of thesis: Mgr. Marek Piliarik, Ph.D.,
Institute of Photonics and Electronics AS CR, v.v.i.

Advisors: Prof. Ing. Ivan Richter, Dr
Department of Physical Electronics, CTU Prague, Faculty
of Nuclear Sciences and Physical Engineering

Abstract:

In recent years, the field of ultrasensitive microscopy has seen significant advancements in its sensitivity and quantitative nature of the readout. Particular for understanding the internal structures of optically thin objects like cells and tissues, quantitative phase sensitivity becomes crucial. This thesis explores new features and implementations in interferometric scattering microscopy (iSCAT), renowned for its non-invasive label-free imaging capabilities. iSCAT's sensitivity to phase changes makes it an ideal method for ultrasensitive phase detection, a pivotal aspect in observing the dynamics of single molecules. This study demonstrates how iSCAT can quantitatively detect the phase of scattered light independent of its amplitude, aiming to advance the accuracy in quantification of macromolecular interactions. The research further investigates how the phase affects iSCAT contrast and reveals that even subnanometer unevenness in coverslips can significantly influence the resulting interferogram. These findings not only underscore the potential of iSCAT in molecular biology but also highlight the necessity for precision in microscopic environments, paving the way for more accurate and reliable microscopic analyses.

Key words: light scattering, iSCAT, ultrasensitive phase detection, single molecule imaging, photothermal spatial light modulator

Contents

1	Introduction	11
1.1	The diffraction limit	12
1.2	Fluorescence microscopy	13
1.3	Interferometric scattering microscopy	14
1.3.1	Application	18
1.4	Mass photometry	20
2	Goals	23
3	Review part	25
3.1	Quantitative phase imaging	25
3.1.1	Interferometry	26
3.1.2	Wavefront sensing	29
3.2	Adaptive optics	31
3.2.1	Liquid crystal spatial light modulators	33
3.2.2	Deformable mirror	34
3.2.3	Digital micromirror device	35
3.2.4	Acousto-optic deflectors and modulators	35
3.2.5	Photothermal spatial light modulator	38
3.3	Influence of subnanometre surface roughness on interference contrast	39
4	Experimental part	43
4.1	Photothermal spatial light modulator development	43
4.1.1	Description of photothermal spatial light modulator	43
4.1.2	The working principle of the photothermal spatial light modulator	43
4.1.3	Manufacture of photothermal spatial light modulator	44
4.2	Characterisation of photothermal spatial light modulator	46
4.2.1	Spatial resolution of photothermal spatial light modulator	46
4.2.2	Response time of photothermal spatial light modulator	47
4.2.3	Absorbance measurement	47
4.3	Phase detection of gold nanoparticles	48
4.3.1	Sample preparation	48
4.3.2	Surface roughness measurement	48
4.3.3	Experiment procedure and setup	48
5	Results	51
5.1	Characterization of photothermal spatial light modulator	51
5.2	Phase detection of gold nanoparticles	53
	Discussion and conclusion	61
	References	63

1. Introduction

Molecules, and in particular biomolecules such as proteins, are the subject of extensive research aimed at unravelling various cellular processes. To achieve this, it is essential to observe their interactions in their environment. Understanding the dynamic behaviour of these molecules is crucial to gaining insight into the sophisticated biological processes that take place in dynamic biomolecular systems, including living cells. The introduction of light microscopy into these investigations is therefore crucial. Unlike electron microscopy or atomic force microscopy, which offer nanometre-level precision, light microscopy allows real-time observation of living samples under room conditions, providing a high temporal resolution. However, this comes at the cost of limited optical resolution.

Despite this restriction, the field of microscopy has witnessed remarkable advancements, leading to the emergence of super-resolution techniques that are capable of surpassing the diffraction limit [1]. Super-resolution microscopy techniques, such as stimulated emission depletion (STED) [2], structured illumination microscopy (SIM) [3] and single-molecule localisation microscopy (SMLM) [4], have transformed the field by enabling imaging of structures beyond the diffraction limit. These techniques achieve resolutions well below the diffraction limit, often reaching the nanometre scale, and thus reveal details of intricate cellular structures [5]. This breakthrough opens up unprecedented opportunities for studying biological and materials science phenomena in unprecedented detail and deepening our understanding of fundamental biological processes.

Super-resolution microscopy methods conventionally rely on fluorescent labels, which introduce certain limitations such as sample perturbations or limited measurement duration [6]. Consequently, there is an increasing focus on the development of label-free microscopy techniques, paving the way for extended real-time super-resolution measurements [7]. In particular, interferometric scattering microscopy (iSCAT) [8] and its quantitative alternative referred to as mass photometry [9] represent straightforward approaches to label-free localisation microscopy, offering single-protein sensitivity and non-invasive high-speed measurements. In addition, iSCAT's inherent sensitivity to phase changes makes it a promising method for precise phase detection in these studies [10].

This thesis describes novel methodology for three-dimensional localization and phase-sensitive detection of extremely small scattering objects such as nanoparticles or single molecules. The methodology for label-free superresolution microscopy based on iSCAT and mass photometry is reviewed, and the main application areas are discussed. The next section is focusing on the experimental aspects of phase information in the measurement of biological samples and describes the concept of quantitative phase imaging. Adaptive optics and various spatial light modulators are introduced, and their application in wavefront correction show a good example

of the importance of phase imaging. The experimental part focuses on ultrasensitive quantitative phase imaging based on iSCAT detection using a new implementation of photothermal spatial light modulator. This method is used to demonstrate the significant effect of sub-nanometre surface roughness on iSCAT contrast measurements.

1.1 The diffraction limit

The main purpose of light microscopy is to magnify objects invisible to the eye. However, the ability to magnify is limited because of the wave nature of light, causing diffraction. The response of the optical system caused by the diffraction of light onto a point object is the three-dimensional distribution of light intensity, called the point spread function (PSF), which appears as a blurred spot. The spatial resolution of the optical system is determined by the size of the PSF [11] and is defined as the minimum distance at which two distinct points emitters can be distinguished. The resolution can be considered in the lateral and axial dimensions.

The diffraction limit can be characterized by the Abbe [12], Rayleigh [13] and Sparrow [14] criteria, depending on the properties and geometry of the PSF. The Abbe limit is defined by

$$d = \frac{\lambda}{2NA}, \quad (1)$$

where d is distinguishable distance, λ is wavelength, and NA is the numerical aperture of the objective defined as $NA = n\sin(\alpha)$, with n being the refractive index of the medium, in which the objective is placed, and α being the half-cone angle of the focused light produced by the objective.

It is very close to the Full Width at Half Maximum (FWHM) diffraction limit of the two overlaying Airy disks which can be derived as

$$d = \frac{0.51\lambda}{NA}. \quad (2)$$

For the Rayleigh limit, the central maximum of one Airy disk overlaps with the first minimum of another. The diffraction limit defined in this way should provide sufficient contrast for the human eye. It is not considered to be a hard limit [15]. The Rayleigh resolution limit is given by

$$d = \frac{0.61\lambda}{NA}. \quad (3)$$

Sparrow's criterion is a less commonly encountered resolution limit. It is characterised by the distance between two point emitters where the overall PSF exhibits a constant intensity level without a dip in intensity at the midpoint. Instead, there is a sustained intensity plateau between the two points. The limited distance is given by

$$d = \frac{0.47\lambda}{NA}. \quad (4)$$

Individual diffraction limits are shown in the Fig. 1.

The axial resolution is a little more complicated. The axial dimension of the Airy disc forms an elliptical pattern because of the nature of the asymmetric wavefront

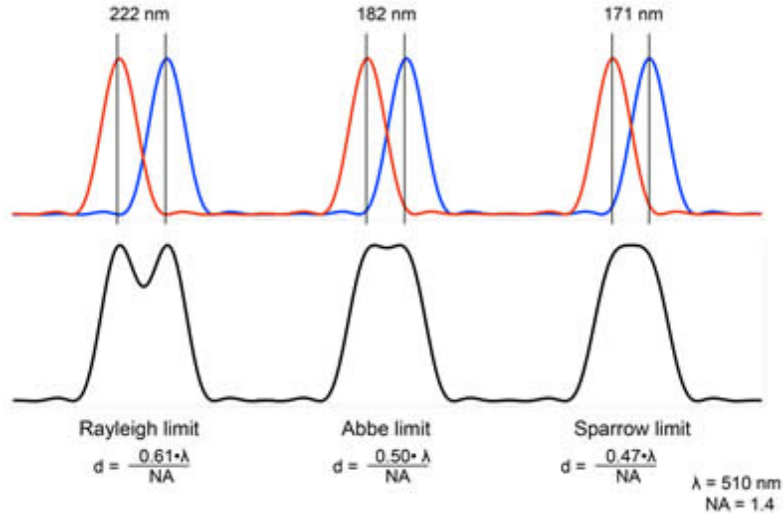


Figure 1: The resolution limits. Three different definitions of resolution limit. Rayleigh, Abbe and Sparrow limit. Image reprinted from [16].

coming out of the microscope objective. To quantify this, the axial resolution limit is given by

$$d = \frac{2\lambda}{NA^2}. \quad (5)$$

The axial width of the PSF is about 2-3 times larger than the lateral width for ordinary high NA objectives. When imaging with visible light ($\lambda \approx 550 \text{ nm}$), the commonly used oil immersion objective with $NA = 1.40$ yields a PSF with a size of $\sim 200 \text{ nm}$ in a lateral orientation and size of $\sim 500 \text{ nm}$ in an axial orientation in a refractive index-matched medium (Fig. 2) [11].

1.2 Fluorescence microscopy

One of the most popular light microscopy techniques enabling single-molecule imaging is fluorescence microscopy using fluorescent labelling. This method allows for detailed real-time observation of the behavior of single molecules. The principle of fluorescence microscopy lies in labelling specific molecules to highlight different cellular structures. After being illuminated by light of one wavelength, the fluorescent label absorbs the light and consequently emits photons with longer wavelengths (i.e., photons with lower energy) that hit the camera.

Fluorescent labels can be made of organic or inorganic materials. Notable inorganic materials for labelling include semiconductor quantum dots (QDs). In 2023, Mouni G. Bawendi, Louis E. Brus, and Aleksey Yekimov were awarded the Nobel Prize in Chemistry for the discovery and development of QDs [17, 18, 19, 20]. Significant advantages of QDs include tunable light emission, high brightness, and resistance to environmental influences. The reason why QDs have not been widely used in biological applications is their toxicity [21]. However, studies are underway to address this issue by modifying the chemical composition [22] or providing a surface coating [23].

Organic fluorophores, such as fluorescent dyes or fluorescent proteins, usually exhibit better biocompatibility than QDs. However, they suffer from low brightness

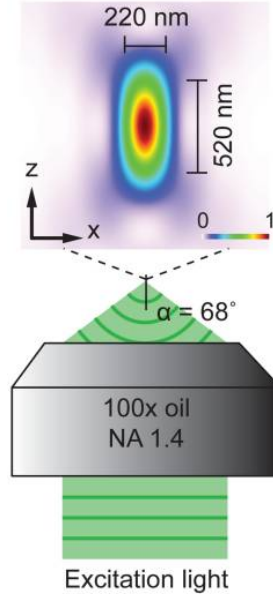


Figure 2: The point spread function. The PSF of a common oil immersion objective with $NA = 1.40$, shows the focal spot of 550 nm light in a medium with refractive index $n = 1.515$. The intensity distribution in the x - z plane of the focus spot is computed numerically and shown in the upper panel, and the FWHM in the lateral and axial directions are 220 nm and 520 nm, respectively. Source: U.S. National Library of Medicine [11].

and unstable emission, and lose their ability to emit light over time as the environment degrades the molecule. This inevitable process is known as photobleaching.

This intricate photophysics of fluorescent dyes or fluorescent proteins is often the main enabling ingredient of modern super-resolution microscopy techniques. Some fluorescence microscopy techniques can achieve resolutions down to tens of nanometres. The stimulated emission depletion microscope (STED) routinely achieves resolutions of 20-30 nanometres [24]. The principle of STED is based on two co-aligned beams: the Gaussian excitation beam and the so-called STED beam. The wavelength of the STED beam is adjusted to de-excite the fluorophores. The phase is designed to generate a doughnut-shaped focal intensity distribution with a 'zero' intensity point in the centre. As a result, only a central focal spot remains active to emit fluorescence. An image obtained using STED is shown in Fig 3 and is compared with the same image obtained using confocal microscopy.

1.3 Interferometric scattering microscopy

Interferometric scattering microscopy (iSCAT) is an advanced nonfluorescent optical microscopy method that uses the interference of scattered and reference light. The significance of iSCAT lies in its ability to detect signals from nanoparticles as small as few nanometers in diameter. Describing the structure and dynamics at the nanoscale is crucial for interpreting the mechanisms of life systems; thus, iSCAT is commonly employed in biological imaging. The concept of iSCAT was first introduced in 2004 by Lindfors et al. [26].

iSCAT microscopy is based on the principles of interferometry and Rayleigh scattering of light at small particles. The illuminating beam enters the microscope objective and illuminates the glass coverslip with the sample. A part of the beam is

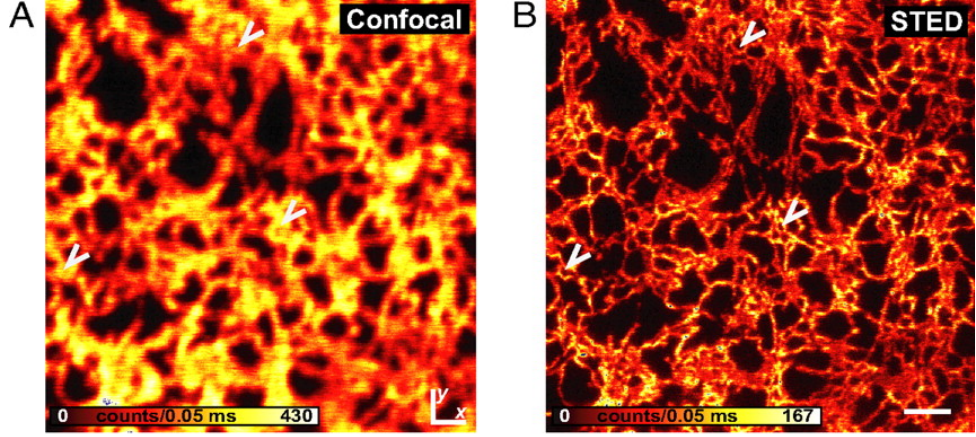


Figure 3: STED. Subdiffraction-resolution imaging of the endoplasmic reticulum (ER) in a living mammalian cell. Shown are confocal (A) and simultaneously recorded (B) STED (x, y) images from the ER marked by the fluorescent protein Citrine targeted to the ER (raw data: 16.3 mW STED focal intensity). Scale bar, 1 μm . The arrows point out rings formed by the tubular network of the ER, which are visible only in the STED image. Adapted from [25].

reflected from the coverslip/sample interface, while the second part passes through the coverslip, and a small fraction of it is scattered on the sample. The reflected and scattered light then pass back through the microscope objective, both following the same optical path and interfering with each other. The final interference pattern is detected on the sensitive camera. The simplified iSCAT setup is shown in Fig. 4.

The complex electric field of scattered and reference light can be written as

$$\mathbf{E}_r = E_r e^{i\phi_r}, \quad \mathbf{E}_s = E_s e^{i\phi_s}, \quad (6)$$

and the intensity of the superposition of the scattered and reference light is given by

$$I = |\mathbf{E}_r + \mathbf{E}_s|^2 = I_r + I_s + 2E_r E_s \cos(\Delta\phi), \quad (7)$$

where $\Delta\phi = \phi_r - \phi_s$ is the phase difference of fields, I_r is the intensity of the reference light, and I_s is the intensity of the scattered light.

The strength of the signal obtained by scattering light E_s depends on the polarisability of the particle α by

$$E_s = \alpha E_i, \quad (8)$$

where E_i is incident light [27]. The polarisability of the spherical particle whose diameter is significantly smaller than the wavelength of the incident light λ is given by the following.

$$\alpha = 3\epsilon_m V \frac{\epsilon_p - \epsilon_m}{\epsilon_p + 2\epsilon_m}, \quad (9)$$

where $\epsilon_{m/p}$ is the complex permittivity of the surrounding medium and particle, respectively, and V is the volume of the particle [28, 29]. The denominator can reach its minimum for metals such as gold or silver. However, the main factor responsible for the magnitude of α is the volume V of the particle. As the size of nanoparticles decreases, the scattering term E_s drops with the third power of the particle diameter

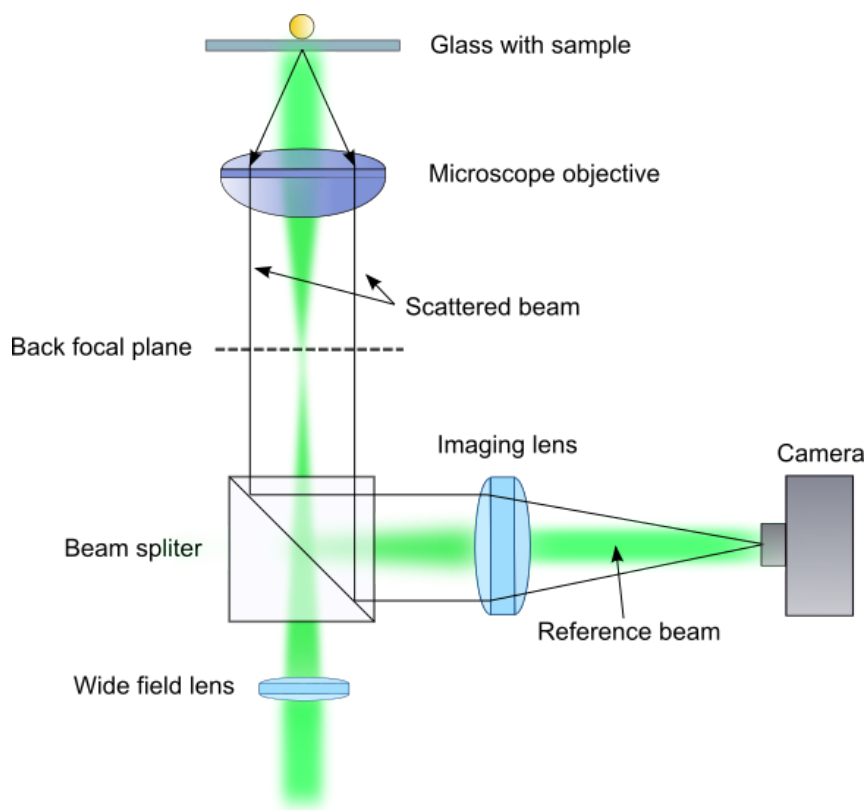


Figure 4: iSCAT set-up. The laser beam is focused on the back focal plane of the objective. The focused beam passes through the beam splitter into the microscope objective and then illuminates the glass-water interface. The part is reflected and forms a reference beam. The rest passes through the interface and part is scattered on the sample. Both scattered and reflected light are collected by the lens and through the beam splitter and the imaging lens illuminates the camera. Their interference can be observed on the camera.

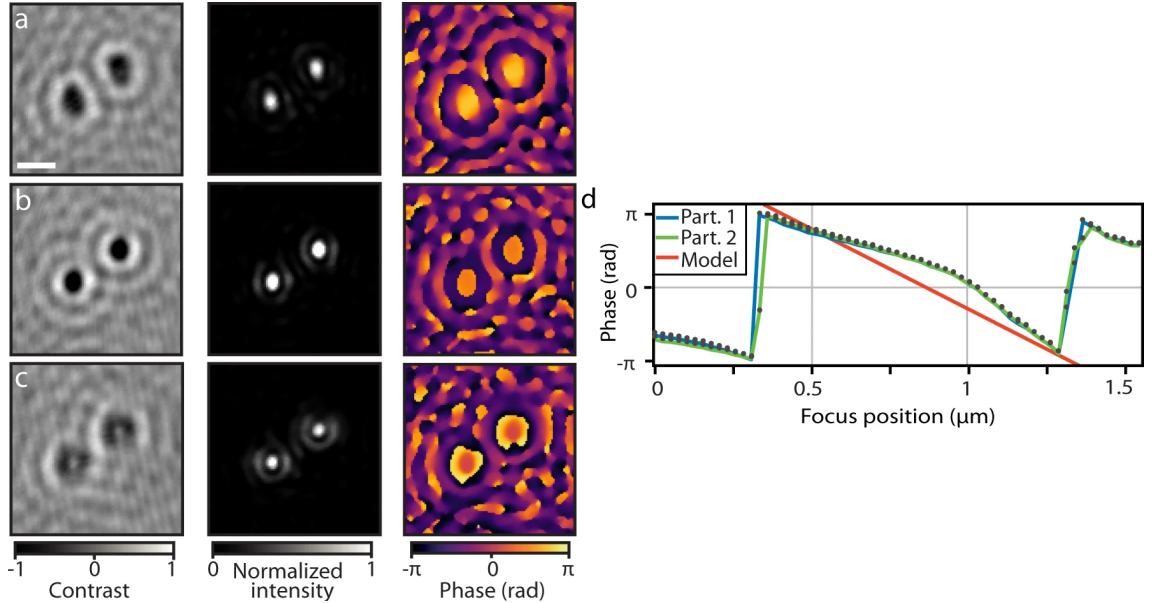


Figure 5: Contrast variation. (a–c) From left to right: iSCAT contrast, reconstructed intensity, and phase image of two gold nanoparticles at the focus positions: (a) $0.35\ \mu\text{m}$ (coverslip closer to the microscope objective), (b) $0.6\ \mu\text{m}$ (best-focus position) and (c) $0.85\ \mu\text{m}$ (coverslip further away from the microscope objective). Representative images out of 50 individual nanoparticles imaged, scale bar indicates $500\ \text{nm}$. (d) Focus position dependence of the phase for the two particles shown in (a–c). A theoretical prediction is shown in red. Adapted from [10].

and thus $I_s = |E_s|^2$ appears negligible [30]. The intensity detected at the camera can then be approximately determined by

$$I \approx I_r + 2E_r E_s \cos(\Delta\phi), \quad (10)$$

and the final image has a contrast

$$c = \frac{I - I_r}{I_r} = \frac{2E_r E_s \cos(\Delta\phi)}{I_r} = \frac{2E_s}{E_r} \cos(\Delta\phi). \quad (11)$$

The contrast of an interferometric image can be varied by changing $\Delta\phi$ which is given by

$$\Delta\phi = \frac{4\pi}{\lambda} n_m z + \phi_{\text{Gouy}}(z') + \phi_{\text{scatt}}(\alpha), \quad (12)$$

where n_m is refractive index of surrounding medium on the coverslip, z is the distance of the particle from the coverslip, ϕ_{Gouy} is Gouy phase accounting for focus position and ϕ_{scatt} is phase of the polarizability of the particle [10]. The change of contrast with the focus position is shown in Fig. 5.

Detection sensitivity, which refers to the ability to distinguish the required object signal from the background signal, is limited by random signal fluctuations known as noise. An important source of noise is the fluctuation in instrumental laser power, which can be addressed through referencing or normalization techniques [27]. The properties of the detector, including dark noise, read noise, and quantum noise (also known as shot noise), impose a limitation on the noise floor [29]. The fundamental limit of shot noise is associated with the particle nature of light. Shot noise

follows the Poisson distribution and depends on the number of photons N as \sqrt{N} . The shot-noise-limited signal-to-noise ratio (SNR) is then given by

$$SNR = \frac{N}{\sqrt{N}} = \sqrt{N}. \quad (13)$$

iSCAT is sometimes referred to as a label-free microscopy method [8, 31]. However, detecting a single protein of nanoscale size is not an easy task. Because the contrast depends on the size of the object as a^3 (where a is the characteristic dimension), even very small power fluctuation or noise from the detector can hinder the detection of the required signal. To enhance the scattering amplitude it is often advantageous to use scattering labels, such as metal or dielectric nanoparticles. Metal labels, such as gold nanoparticles, are employed to label small samples, such as single proteins. Gold nanoparticles (GNPs) provide good contrast due to their relatively high polarisability compared to single proteins and are frequently used in iSCAT measurements owing to their biocompatibility.

1.3.1 Application

Due to its excellent detection sensitivity, iSCAT has proven to be a crucial tool in a variety of studies such as direct detection of single unlabelled proteins [8], high-speed single particle tracking with nanometer localization precision [32], or quantitative mass photometry of single molecules [9].

In 2016, researchers utilized iSCAT technology to track individual molecules in a study that unveiled compartmentalized diffusion in living cells [33]. The measurement achieved 3 nm spatial precision and up to 25 μ s temporal resolution. 40 nm GNPs were used as labels during the tracking of membrane proteins in the plasma membrane of live cultured mammalian cell lines and neurons of the hippocampal. There was evidence of restricted diffusion at the membrane.

Fast processes, such as protein movements and molecular interactions at the nanoscale, typically occur on a rapid milli- to microsecond scale. However, these events are not always detectable using commonly used fluorescence microscopy. iSCAT, on the other hand, can capture up to 1 million frames per second. The study conducted by Spindler et al. in 2016 [32] introduced different tracking speeds. With a temporal resolution of 1 ms (1 kHz frame rate), they demonstrated the tracking of lipids labelled with 20 nm GNP with a localization precision better than 2 nm. This enabled the observation of the transient confinement of individual lipid molecules within regions as small as 10 nm. They further compared the measured trajectory of lipids labelled with 5 nm GNPs recorded at a frame rate of 23 kHz and the trajectory of 20 nm GNPs bound to lipids recorded with a high-speed camera at a speed of 913 kHz. The difference between trajectories is shown in Fig. 6. The trajectory measurement with the higher speed was almost three times shorter, but Fig. 6b shows that it is significantly fuller. This is due to the fact that higher speeds reveal confinements that were previously missed.

iSCAT has proven to be an effective method for imaging single molecules. However, when studying more complex samples, such as biological cells, the superposition of scattering signals from different sources, especially those along the optical axis of the microscope objective, complicates data interpretation. This challenge led to the introduction of confocal iSCAT and spinning disc confocal iSCAT techniques [34, 35].

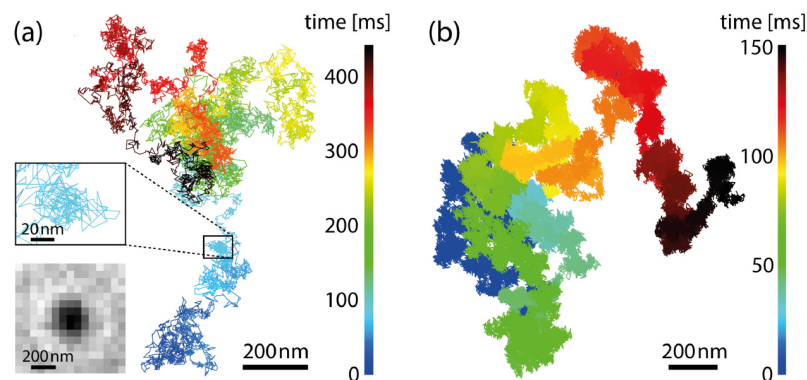


Figure 6: High-speed tracking of lipid diffusion using a GNP as label. (a) Trajectory of a 5 nm GNP bound to a biotinylated DOPE lipid via streptavidin in a DOPC SLB recorded at 23 kHz frame rate for 0.44 s. The localization precision is 5 nm. (b) Trajectory of a 20 nm GNP bound to a biotinylated DOPE lipid in a DOPC SLB recorded at 913 kHz for 0.152 s. The localization precision is 9.7 nm. Adapted from [32].

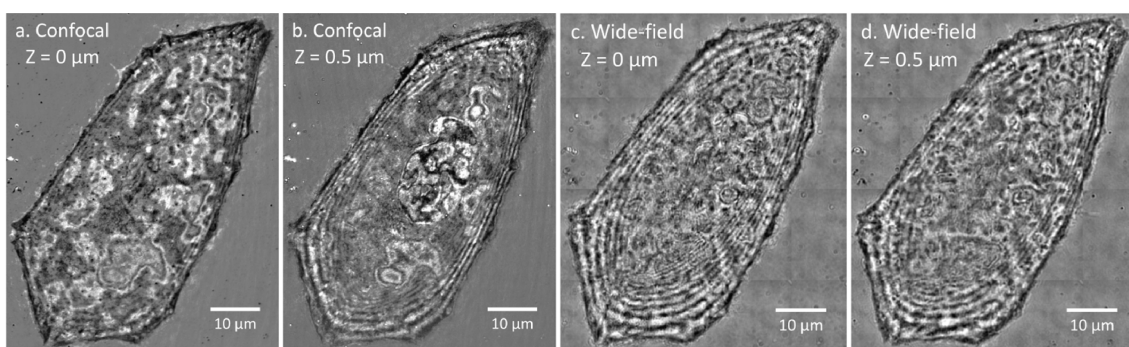


Figure 7: The comparison between the confocal and wide-field iSCAT images of a biological cell. (a,b) The iSCAT confocal image of a U2OS cell at $z=0\ \mu\text{m}$ (a) and $z=0.5\ \mu\text{m}$ (b). See the z stack video of the cell in Visualization 4. (c,d) The iSCAT wide-field images of the same cell shown in (a) and (b) acquired at the corresponding axial positions, i.e., $z=0\ \mu\text{m}$ (c) and $z=0.5\ \mu\text{m}$ (d). While the two confocal images (a) and (b) display distinct features because of the optical sectioning, the two wide-field images (c) and (d) show similar features as the result of a lower axial resolution. Adapted from [35].

In confocal microscopy, a pinhole aperture is used, allowing only light from the focal point of the sample to pass through. This results in a clear and focused image while blocking light scattered outside of the focal volume. iSCAT’s confocal mode provides sensitive label-free 3D imaging, eliminating out-of-focus light and enabling imaging of nanostructures down to a depth of about $4\ \mu\text{m}$.

The spinning disc confocal iSCAT is an alternative configuration of the confocal iSCAT with a spinning disc apparatus. This setup includes one disc with microlenses and a second disc with pinholes. The rotation of these discs ensures that the laser light is rapidly scanned across the entire field of view, enabling fast image acquisition. The maximum rotation speed of the disc is up to 10,000 rpm, allowing for the capture of multiple frames in a single rotation.

1.4 Mass photometry

Mass photometry, originally introduced as interferometric scattering mass spectrometry [9], is a label-free light microscopy technique that enables quantitative *in vitro* measurement of the mass of single molecules and their interactions and processes, such as cross-linking, aggregation, and polymerization, with the high resolution.

Mass photometry is a quantitative option for iSCAT, which determines the mass of the sample based on its relation with the optical contrast. The polarizability α (Eq.9) and hence the amplitude of the scattered field E_s is proportional to the volume of particles and scales with the permittivity and thus the refractive index ($n = \sqrt{\epsilon_r \mu_r}$).

The principle of mass photometry operation is that, at a low concentration in solution, the sample diffuses and adsorbs non-specifically to the microscope coverslip/solution interface, as illustrated in Fig. 8A. By recording the interference of reflected light from the interface and scattered light from the adsorbed molecule, individual binding events can be quantified. The interferogram is shown in Fig. 8B. From the contrast of the interferometric scattering, it can be determined how many units the oligomer consists of. The contrast change of the bound monomer, dimer, trimer, and tetramer is depicted in Fig. 8C where the molecule under investigation was bovine serum albumin protein (BSA). From this measurement, it was shown that the scaling between mass and interferometric contrast is linear, which was supported by further measurements with different proteins varying in mass from 53 to 803 kDa [9]. In measurement, a 19-kilodalton resolution and 1-kilodalton precision were achieved.

Mass photometry has been shown to be an accurate technique for the detection and imaging of nucleic acids. It has proven to be a novel analytical approach for studying protein-DNA interaction at the single-molecule level. A linear relationship between the number of bases in a DNA molecule was identified, allowing quantification of DNA length with 2 base pairs accuracy. The dependence of optical contrast on the shape and orientation of the molecule, such as short DNA strands illuminated with linearly polarized light, has recently been demonstrated [36]. The simulation with differently oriented BSA molecules showed that there is almost no dependence on the shape of the molecule when illuminated with circularly polarized light, whereas when illuminated with linearly polarized light, there is a detectable deviation for different orientations of the molecule. The result histograms are shown in Fig. 9.

Mass photometry has also become a powerful method for studying membrane-associated biomolecular processes as it can provide tracking of individual oligomers while simultaneously measuring their mass [37]. This variant is referred to as dynamic mass photometry.

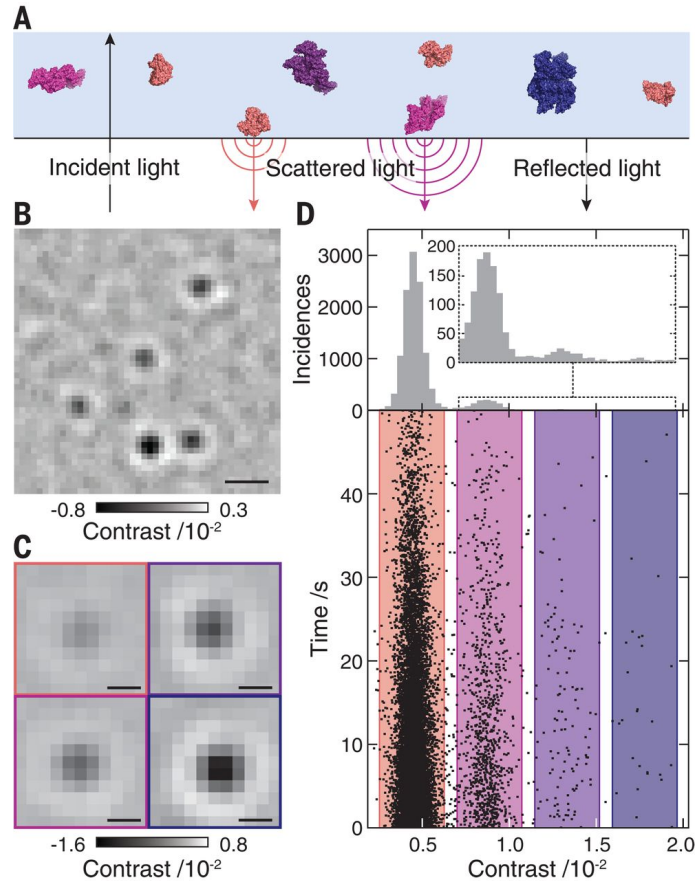


Figure 8: Interferometric scattering mass spectrometry. (A) Schematic of an experimental approach based on immobilization of individual molecules near the glass slide. (B) Differential interferometric scattering image of BSA. Scale bar, 0.5 μm . (C) Representative images of monomers (top left), dimers (bottom left), trimers (top right), and tetramers (bottom right) of BSA. Scale bars, 200 nm. (D) Scatter plot of single-molecule binding events and their scattering contrasts for 12 nm BSA (lower panel). Corresponding histogram ($n = 12,209$) with a zoomed-in view of the region for larger species (upper panel). The reduction in landing rate results from a drop in BSA concentration. From [9]. Reprinted with permission from AAAS.

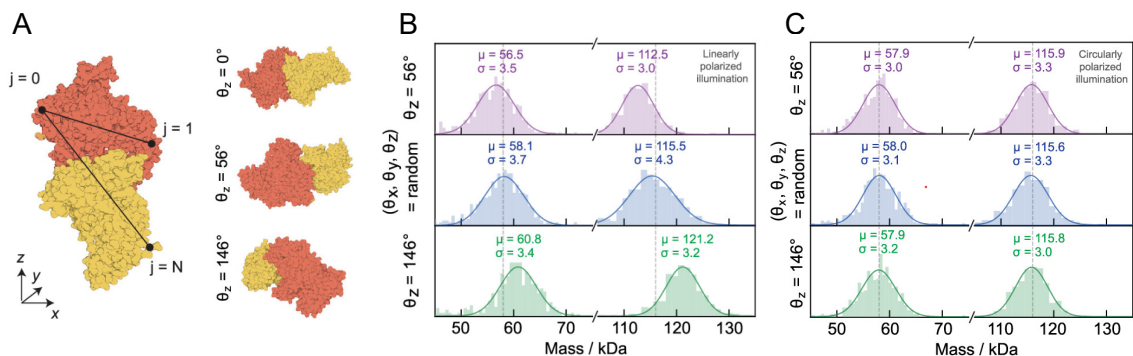


Figure 9: Dependence of mass measurement on biomolecular shape. (A) Modeling the shape and orientation of a protein, here the dimer of BSA. (B) Mass histograms for a simulated landing assay where all BSA monomers (or dimers) land with the same (fixed) orientation ($\Theta_z = 56^\circ$; $\Theta_z = 149^\circ$), or with random orientations, while being illuminated with linearly polarized light. (C) Same simulation as in (B) except for circularly polarized illumination. Adapted from [36].

2. Goals

The main goal of the thesis is to advance and test ultrasensitive quantitative phase imaging in the interferometric scattering microscopy setup and demonstrate its applicability to resolve origins of the contrast uncertainty of an individually detected scattering nanoparticle in the proximity of a weakly scattering surface. To do that, I focus on the following sub-objective in the thesis:

- I collect and review relevant literature on interferometric scattering microscopy (iSCAT), mass photometry and wavefront shaping. The focus is on comparing the performance limits and various experimental implementations.
- In the experimental part, I optimize the phase detection of iSCAT microscopy, identify its limits, and develop a new generation of the photothermal spatial light modulator element.
- I demonstrate the newly developed methodology to detect a large set of single scattering nanoparticles and discern their scattering phase and the scattering amplitude. I show, how the scattering environment within the near-field radius affects the uncertainty of the scattering phase and consequently the accuracy of the amplitude measurement.

3. Review part

3.1 Quantitative phase imaging

The phase of a light wave is a dimensionless quantity that defines the relationship between the intensity of the electric field at a given spatio-temporal coordinate and the reference state at the point of origin. The challenge in imaging optically thin specimens, such as living cells or proteins, lies in their minimal absorption or scattering of visible light, allowing a significant amount of incident light to pass through the translucent sample.

One way to improve the imaging of these objects is to tag them with a fluorescent label. However, this is not always desirable due to issues such as photobleaching, photoblinking, or chemical reactions. Another approach to enhancing contrast is to utilize the phase of the incident light. When imaging weakly scattering objects, it is the phase change rather than the amplitude that carries crucial information about the internal structure. These objects are, therefore, referred to as 'phase objects'.

In the 1930s, Frits Zernike [38] recognised the importance of phase and developed Phase Contrast Microscopy (PCM), in which the contrast of the interferogram produced by scattered and unscattered light is enhanced by introducing a $\pi/2$ phase shift between the two optical fields. At the time, PCM represented an advanced approach to imaging and revealing the internal details of transparent specimens without the need for staining. Figure 10 shows an example of a PCM image. In cell imaging, PCM is more effective than brightfield and darkfield in increasing contrast.

Another widely used qualitative method for imaging phase objects is Differential Interference Contrast (DIC) microscopy, also known as Nomarski microscopy. This method uses a pair of Wollaston prisms to split the polarised beam and then recombine it after passing through the sample. The formation of an interference pattern is attributed to a phase shift induced by the varying thickness of the sample.

Both PCM and DIC microscopy are suitable for label-free imaging of cells and other phase objects. However, the phase information is coupled nonlinearly in an intensity distribution. Therefore, it cannot be retrieved quantitatively and PCM and DIC remain a qualitative method [39, 40].

Conventional photodetectors only detect the distribution of the light intensity and are unable to capture the phase information due to rapid fluctuations. Therefore, additional optics and computation are required to extract the phase information. Quantitative Phase Imaging (QPI) is a collection of methods that quantify a phase shift while imaging weakly scattering and absorbing samples. QPI has evolved into a remarkable and practical 3D imaging method. Its high sensitivity, label-free imaging, and quantitative measurements make it suitable for studying biological structures, which has applications in medical and industrial research, especially in diagnostics. QPI performs quantitative measurements of refractive index and thickness and al-

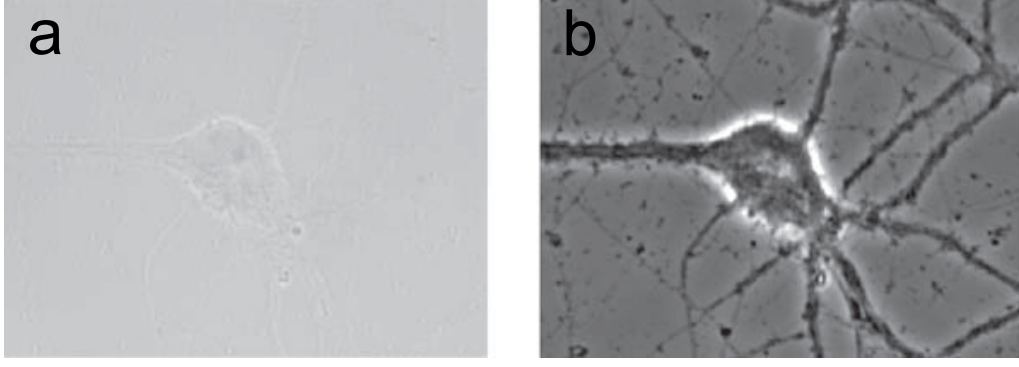


Figure 10: PCM. Difference between (a) bright field and (b) phase contrast microscopy. Image of an unstained neuron. Reprinted from [39].

lows reporting on the morphology of living cells, which changes significantly due to viral diseases or cancer.

3.1.1 Interferometry

Interferometry is a technique that combines and analyzes multiple waves to extract information about their properties. Wave interference occurs when two or more waves overlap, resulting in the amplification or cancellation of certain parts of the waves.

In an interferometric measurement, an image field is combined with a reference field, and their interferogram is observed to obtain phase information [41]. Interferometry is therefore one of the common quantitative phase imaging (QPI) methods used to access the phase difference of the light passing through the sample of interest.

Both transmission and reflection QPI systems have been developed [42], nevertheless, there is a fundamental difference in the phase measuring in transmission and backscattering geometry. Assuming that the field in the medium can be approximated by the incident field (which is assumed to be a plane wave along z direction)

$$U_0(r, \omega) = A(\omega)e^{in_0\beta_0z}, \quad (14)$$

where A is the amplitude of incident light, ω the angular frequency, n_0 the refractive index in the background, $\beta_0 = \frac{\omega}{c}$ (with c being the speed of light in vacuum), then the total scattered field in the inhomogeneous environment is given by the Helmholtz equation

$$\nabla^2 U_1(r, \omega) + n_0^2 \beta_0^2 U_1(r, \omega) = -\beta_0^2 \chi(r, \omega) U_0(r, \omega), \quad (15)$$

where U_1 is the scattered field and $\chi = n^2(r, \omega) - n_0^2$ (where $n^2(r, \omega)$ is the local refractive index) the scattering potential. The scattered field has two components U^+ and U^- that propagate along $+z$ (forward scattering) and $-z$ (backscattering). The final equations for small phase shifts for transmitted and backscattered fields are

$$U_f(r_\perp, z) = Ae^{i\beta z} e^{-i\beta[\bar{n}(r_\perp) - n_0]L} \quad (16)$$

$$U_b(r_\perp, z) = Ae^{-i\beta z} e^{i\beta \int_{-L/2}^{L/2} [n(r_\perp, z) - n_0] e^{i2\beta z} dz} - Ae^{-i\beta z} \quad (17)$$

where $U_f = U_0 + U^+$ is the transmitted field, U_b is the back-scattered field, $\bar{n}(r_\perp)$ is the longitudinally averaged refractive index, $n(r_\perp, z)$ is the longitudinal refractive

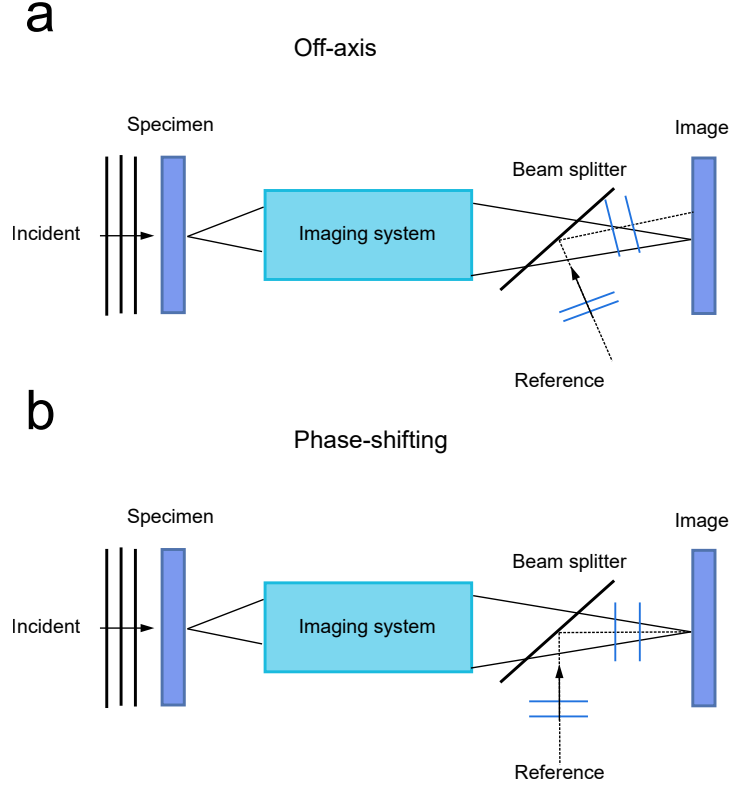


Figure 11: Two configurations of QPI. (a) Schema of off-axis method: the referenced field is tilted with respect to the imaging field. **(b)** Schema of phase shifting method: the referenced field is parallel with the imaging field. Adapted from [39].

index at z position and L the sample thickness [42]. While in transmission geometry, phase shift relates linearly to the sample thickness and refractive index difference, the situation in back-scattering is much more complicated as the field contains high spatial frequencies due to the superposition of plane waves back-scattered from various depths in the sample. The relationship between the phase, thickness, and refractive index of the sample is completely obscured, which makes it impossible to infer quantitative morphology or topography information from a reflection phase image alone [30, 42].

The image field in transmission microscopy can be expressed as a function of time and space

$$U_i(x, y, t) = |U_i(x, y)|e^{-i(\langle\omega\rangle t - \langle\mathbf{k}\rangle \cdot \mathbf{r} + \phi(x, y))} \quad (18)$$

where $|U_i(x, y)|$ is the magnitude of the field, $\langle\omega\rangle$ the central frequency, $\langle\mathbf{k}\rangle$ the central wavevector and ϕ the phase of the interest. After the interference between the imaging field U_i and the reference field U_R , the intensity on the detector is as follows

$$I(x, y, t) = |U_i(x, y)|^2 + |U_R|^2 + 2|U_i(x, y)||U_R| \cos[\langle\omega\rangle(t - t_R) - (\langle\mathbf{k}\rangle - \mathbf{k}_R) \cdot \mathbf{r} + \phi(x, y)] \quad (19)$$

where $|U_R|$, t_R and \mathbf{k}_R are the amplitude, time delay, and wavevector of the reference field, respectively [30]. Depending on whether t_R or \mathbf{k}_R is modulated, the QPI is divided into two configurations: *off-axis* interferometry and *phase-shifting* interferometry.

Phase-shifting configuration

The phase-shifting configuration produces an image in the focal plane by using in-line geometry, where the referenced beam propagates towards the image plane parallel to the imaging beam. The scheme is illustrated in Fig. 11b. The final intensity of this configuration is

$$I(x, y, t) = |U_i(x, y)|^2 + |U_R|^2 + 2|U_i(x, y)||U_i(x, y)|\cos[\phi(x, y) + \delta] \quad (20)$$

where $\delta = \langle \omega \rangle (t - t_R)$ [30]. A phase map can be acquired by recording 4 intensity images with different phase shifts ($\delta = 0, \pi/2, \pi, \pi/3$) as

$$\phi(x, y) = \arg[I_0 - I_\pi, I_{3\pi/2} - I_{\pi/2}]. \quad (21)$$

Phase-shifting offers several advantages, including the preservation of diffraction-limited transverse resolution, reduction of spatial noise, and straightforward reconstruction of the phase map using simple mathematical operations. However, it is limited by the necessity of acquiring multiple images sequentially [43]. Microscopic techniques that employ the phase-shifted QPI regime include Digital Recorded Interference Microscopy with Automatic Phase Shifting (DRIMAPS) and optical quadrature microscopy (OQM).

DRIMAPS is made up of the optically similar arms of the Mach-Zehnder interferometer. The first arm contains the sample, while the second arm contains the dummy sample and the optical wedge that provides the phase shift. By changing the phase shift in the second arm by $\pi/2$ each time, 4 recorded intensity frames are obtained. The OQM system also utilizes a Mach-Zehnder interferometer, where the linear polarization in one arm is transformed into circular polarization, and the sample is placed in the second arm. Upon rejoining the beams, the phase shift can be determined by rotating the analyzer.

The spatial light interference microscopy (SLIM) is an advanced highly sensitive QPI method. It is a phase-shifting interferometer built onto a phase-contrast microscope using white light as a source of illumination. SLIM produces spatial modulation by introducing a reflective liquid crystal phase modulator which additionally generates further $\pi/2$ phase shifts. By combining four images, each for $\pi/2$ phase shift, one can produce a quantitative phase image. SLIM is suitable for combination with fluorescence imaging and for sub-nanometre cell dynamics imaging, as it provides spatially and temporally sensitive quantitative measurements [44]. The principle of SLIM and the SLIM phase image of a neuron are shown in Fig.12. SLIM can compete with atomic force microscopy (AFM) as an effective tool for topography measurement. Compared to AFM, it is completely contactless, much faster (three orders of magnitude) and provides nanoscale accuracy, which allows the topography of single atomic layers to be revealed [39, 45].

Off-axis configuration

With off-axis geometry, the direction of the referenced field is inclined to the incident field, and both reach the image plane simultaneously without delay. The scheme is illustrated in Fig. 11a. The resulting intensity is

$$I(x, y, t) = |U_i(x, y)|^2 + |U_R|^2 + 2|U_i(x, y)||U_i(x, y)|\cos[(\Delta k \mathbf{r} + \phi(x, y))] \quad (22)$$

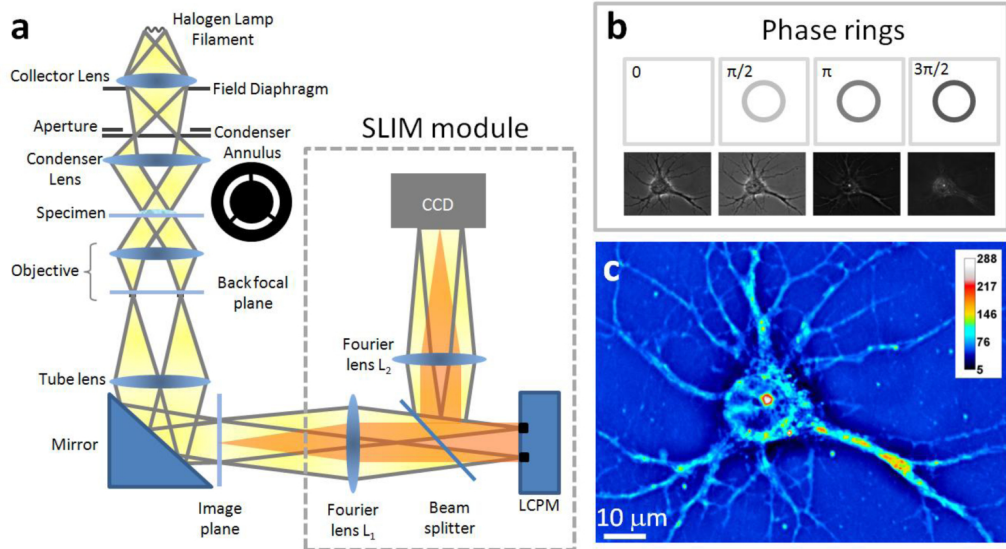


Figure 12: SLIM principle. (a) Schematic setup for SLIM. (b) The phase rings and their corresponding images recorded by the CCD. (c) SLIM quantitative phase image of a hippocampal neuron. Reprinted with permission from [44] © The Optical Society.

where $\Delta k = \langle \mathbf{k} \rangle - \mathbf{k}_R$ which determines the rate of the wavevector difference between the two fields [30]. The cosine term is interpreted as the real part of a complex analytic signal and the corresponding imaginary part is obtained via the Hilbert transform. The phase hidden in the argument of the trigonometric functions is then obtained as

$$\phi(x, y) + \Delta k \mathbf{r} = \arg[\cos(\Delta k \mathbf{r} + \phi), \sin(\Delta k \mathbf{r} + \phi)]. \quad (23)$$

The advantage of off-axis methods is single frame shot capability, which allows fast acquisition rates [46]. Microscopy methods that work in the off-axis configuration are Digital Holography Microscopy (DHM) [47] or Hilbert Phase Microscopy (HPM) [48].

DHM uses the Mach-Zehnder interferometer where the beam is split into two separate paths. In the first path, the sample is placed and the object is imaged by the microscope objective on the charged coupled device (CCD), which is located at a set distance from the image plane so that it records an out-of-focus field. The two paths are connected by a beam splitter which is at a certain angle, causing the off-axis alignment between the imaging beam and the reference beam. DHM exists also in phase-shifting configuration [49]. After recording the interferogram, the numerical Fourier transform is applied to reconstruct the hologram. DHM provides accurate intensity and phase distribution simultaneously without mechanical scanning and has high temporal resolution, but as an interferometric approach is sensitive to noise from a reference arm. HPM is very similar to DHM, but instead of recording the interferogram in a out-of-focus plane, it is recorded directly in the image plane [39].

3.1.2 Wavefront sensing

Wavefront sensing describes methods that aim to recover the aberrations in a wavefront caused by phase delays within a sample. There are two techniques that differ in the way they obtain information about the wavefront: direct and indirect [50].

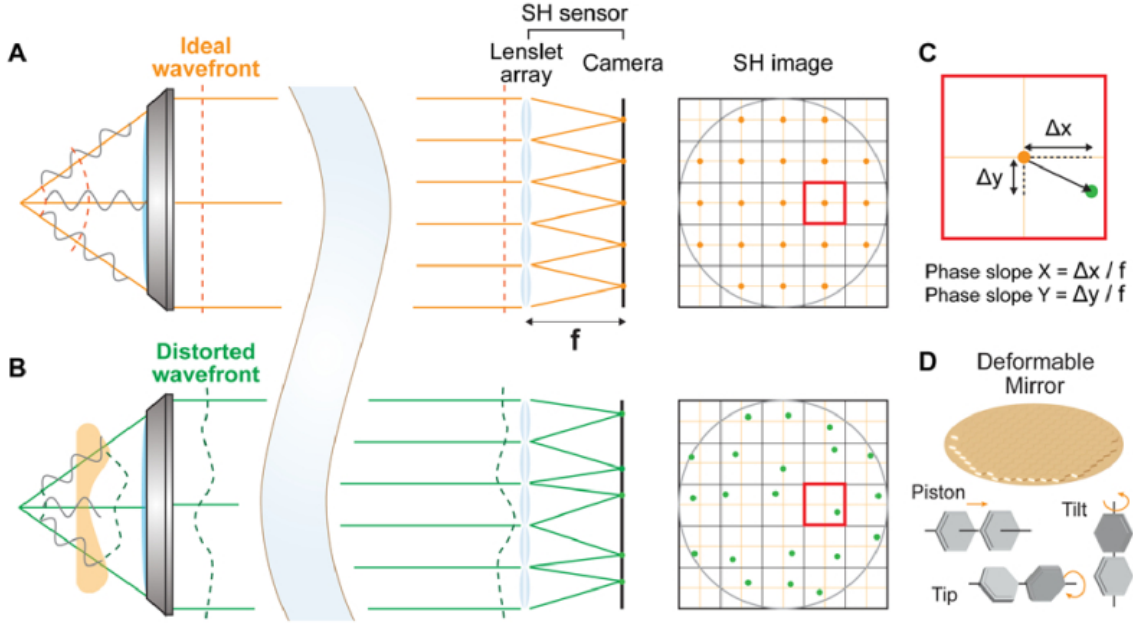


Figure 13: Principle of the Shack-Hartmann (SH) sensor. (A, B) An ideal wavefront (A) and distorted wavefront (B) measured by an SH sensor. (C) 2D local phase gradients calculated from displacements of a segmented focus. (D) Wavefront correction with a deformable mirror with each segment controls piston, tip, and tilt. Adapted from [50].

In direct wavefront sensing, the wavefront itself is directly measured and analyzed without relying on any additional information or supplementary measurements. A commonly used direct wavefront sensor is the Shack-Hartmann (SH) wavefront sensor [51, 52]. The key idea is to split the incoming wavefront into many small sub-apertures and then measure the local tilt or slope of each sub-aperture to determine the overall wavefront shape. The most important part of the SH wavefront sensor is a mask with a microarray of lenses. Each lenslet corresponds to a sub-aperture that samples a portion of the incoming wavefront. The lenslet focuses the light onto a detector, and the position of the focused spot on the detector is related to the local tilt or slope of the wavefront within that sub-aperture. If the wavefront is parallel to the camera, the light will be focused at the center of the sub-aperture. If the wavefront is tilted, the spot is off-center. The shape of the incoming wavefront is then calculated from the measured position of the focused spot. The principle of the SH wavefront sensor is shown in Fig. 13.

The SH wavefront sensor provides highly sensitive real-time continuous wavefront measurement. It is relatively simple in design and operation, making it suitable for a wide range of applications. On the other hand, SH sensors have reduced accuracy for very high-order aberrations or complex wavefronts, have lower spatial resolution, and provide less detailed information about the full wavefront shape. Another drawback of direct wavefront sensing is the requirement for minimal scattering of the light used. This is particularly challenging in highly scattering tissues, where the signal used for wavefront sensing is reduced by scattering and hidden by an enhanced diffuse background [40, 50]. A powerful alternative to the SH sensor is the quadriwave lateral shearing interferometry (QWLSI). QWLSI uses a modified Hartmann mask with a 2D diffraction grating [53].

Another frequently used wavefront sensor, for example in astronomy, is the pyramid sensor [54]. The incoming beam is split at the apex of the pyramidal prism.

For example, a four-sided pyramid produces four pupil images. For an unaberrated wavefront, the four images are identical. In the case of aberration, the intensity distribution of the pupil images changes. The intensity distribution in the pupil images allows the acquisition of local wavefront gradients. The estimated wavefront gradients can then be used to estimate wavefront aberrations. The pyramid sensor has a higher sensitivity than the SH sensor. However, it suffers from strong non-linear behaviour.

Indirect wavefront sensing techniques do not directly measure the wavefront itself but rely on secondary measurements or information to derive the wavefront properties. Indirect methods involve simpler hardware implementations than direct sensing systems, but the software configuration for these systems can be more complicated [55]. Indirect methods can measure an effect that is affected by the wavefront aberrations and then use mathematical or computational methods to estimate the aberrations indirectly. One of the indirect techniques is modal wavefront sensing [56]. It works by representing the distorted wavefront as a combination of specific mathematical modes, typically Zernike polynomials. These modes describe different types of aberrations such as defocus, astigmatism, coma, spherical aberration, and other distortions. In modal wavefront sensing, a bias aberration is added to the aberrated wavefront of interest. By applying appropriate bias aberrations, it is possible to estimate the magnitude of each Zernike component in the input wavefront. Modal wavefront sensors can characterize a wide range of wavefront aberrations, including both low and high-order distortions, and provide detailed wavefront analysis. However, implementing modal wavefront sensing can be more challenging, requiring additional computational processing. It also relies on a predefined set of aberration modes (e.g., Zernike modes), which may not cover all possible wavefront distortions. It also does not provide real-time measurements and is not well-suited for dynamic aberration correction compared to SH sensors.

3.2 Adaptive optics

Adaptive optics (AO) is a collection of technologies typically used in astronomy [57, 58] or microscopy [59, 60, 61, 50] to measure and correct optical aberrations. Optical aberrations are imperfections or deviations from ideal optical behavior in telescopes or microscopes. These aberrations can lead to distortions and image degradation, affecting the quality of observations and the ability to resolve fine details in astronomical objects or microscopic samples. Understanding and minimising these aberrations is critical to achieving high-quality observations and measurements in both astronomy and microscopy. There are several types of optical aberrations encountered in astronomy and microscopy: chromatic and spherical aberrations, coma, astigmatism, field curvature, atmospheric aberrations caused by the Earth's atmosphere, aberrations in immersion media, or aberrations caused by refractive index inhomogeneities in thick biological samples. The example of correction of atmospheric aberration is shown in Fig. 14. The aim of AO is to apply a deformation to the optical system that is exactly equal in magnitude but opposite in sign to the aberrations present in the wavefront, in order to correct the aberrations and achieve diffraction-limited image quality with maximum signal [62].

AO is a combination of electro-optical and computational techniques. It consists of three primary components: a sensor to measure aberrations, a corrector to

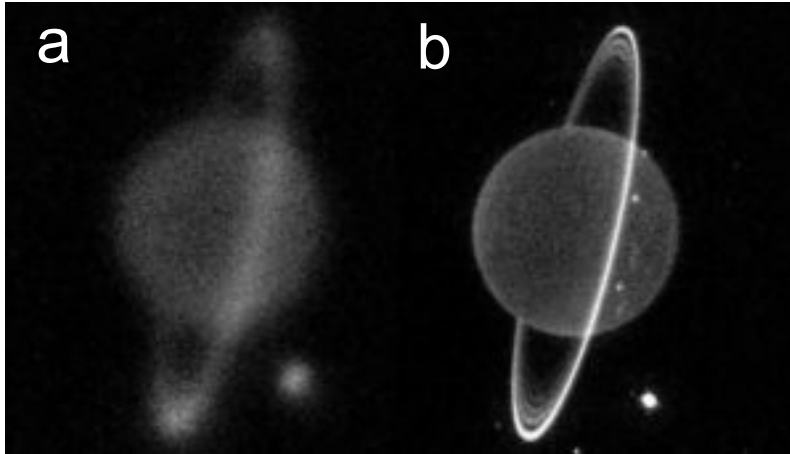


Figure 14: Uranus. The near-infrared images of Uranus without adaptive optics (a) and with adaptive optics (the Keck telescope’s adaptive optics system) (b). Image Credit: Heidi Hammel and Imke de Pater.

compensate for these aberrations, and a controller responsible for calculating the necessary signals sent to the corrector based on the sensor measurements. Typically, the corrector and sensor are positioned conjugate to the pupil plane of the imaging system [62].

To implement AO effectively, it is important to consider the characteristics of the aberrations that need to be corrected. This involves identifying the type of aberrations present and understanding how quickly the wavefront changes shape over time. Such considerations are critical in tailoring AO systems to the unique characteristics and requirements of each application.

There is a wide range of approaches to achieving both wavefront sensing and wavefront correction. In addition, the specific implementation requirements can vary significantly in the different fields where AO is applied. The variation in implementation requirements and aberration characteristics can make it difficult to translate concepts and methods across different applications.

Fast and effective feedback is a critical parameter in this area, as it is essential to correct the wavefront as quickly as possible. For aberration correction, it is necessary to first measure the distorted wavefront and, after calculating the optimal wavefront correction, send feedback to the AO device to compensate for the aberration and create a smoother point spread function coming from the focus [63]. The principle of aberration correction is shown in Fig. 16. When adaptive optics are used in microscopy, prolonged aberration measurements can lead to bleaching of the biological sample, so it is important to find an optimal correction control loop. Speed is also crucial to keep up with any change in aberration over time.

Spatial light modulators (SLMs) are dynamic devices that are often used for active correction of optical aberrations. After detecting the aberration, the aberration correction is calculated and the instruction is sent to the SLM. SLMs modify the amplitude, phase, polarisation, or direction of the wave and are therefore recognised as useful devices with various applications in microscopy [64], astronomy [65, 58] or holography [66]. Frequently used SLMs include liquid crystals [67, 64], deformable mirrors [68], metamaterials [69], or photothermal SLM [70, 10].

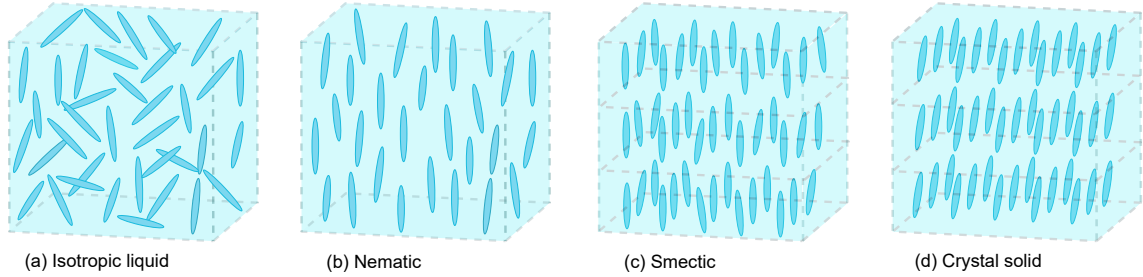


Figure 15: Liquid crystals phases. Phases according to positional order and orientation of molecules. (a) Isotropic liquid where molecules have no positional or orientation order. (b) Nematic phase where molecules are partially oriented but do not have positional order. (c) Smectic phase where molecules have partial orientation and positional order. (d) Crystal solid is the last phase where there are either positional or orientation orders. Adapted from [73].

3.2.1 Liquid crystal spatial light modulators

Liquid crystal (LC) is a material composed of organic anisotropic rod-like (or disk-like) molecules that exhibit the physical properties of both solids and amorphous liquids. A direct consequence of the ordering of the molecules in an LC is optical anisotropy [71]. Transitions between solid and liquid phases can occur in two different ways: first by purely temperature change and second by both concentration and temperature change. The LC of the first type is called "thermotropics," and the second type is called "lyotropics" [72].

Depending on the temperature, thermotropic LC exhibits different phases. At high temperatures, the molecules of the LC are in a liquid state and can move around freely. (Fig. 15a). As the temperature decreases, the molecules enter the nematic phase, which is the most common and simplest LC phase. The molecules are partially oriented in a defined direction perpendicular to the surface, but have no positional order (Fig. 15b). They are used as optical modulators and in displays (LCDs). The next phase is smectic LC, which is structured in layers in which the molecules have a partial orientation order (Fig. 15c). In the last phase at low temperature, the crystal is in the solid phase (Fig. 15d) [73].

The LC SLM devices can operate in two modulation modes: amplitude modulation and phase modulation. Amplitude modulation is achieved by applying the voltage and varying the direction of linear polarization of light passing through a linear polarizer. Phase modulation is achieved by electrically changing the refractive index along the optical path.

The most commonly implemented type of LC SLM is the twisted nematic (TN) modulator. The LC material is sandwiched between two glass plates. The plates are oriented so that their preferred orientations are perpendicular to each other. At zero voltage, this results in a twisted orientation pattern of the molecules. Molecules close to one surface are oriented according to their preferred direction, and as they move towards the other glass surface, the orientation is rotated more and more towards the preferred molecular orientation of that surface [74]. Another type is liquid crystal on silicon (LCoS). A two-dimensional array of liquid crystal modulators is fabricated on a silicon complementary metal oxide semiconductor (CMOS) backplane. This backplane consists of the electronic circuitry that is buried underneath pixel arrays. An LCoS device can be either transmissive or reflective and can be

used to change the polarization or phase of an incident light beam by exploiting the electrically modulated optical properties of LC and the high-performance technology of CMOS [75].

Due to its affordable price, high spatial resolution, large bandwidth, and low power consumption, the LC modulator has become a popular device for modulating intensity, phase, and polarisation state. However, they are among the slowest optical modulators. The refresh rate is typically in the order of hundreds of Hz. This limitation is due to the time required for the molecules to reorient, which sets a relatively slow rate for these processes, typically a few milliseconds [74].

3.2.2 Deformable mirror

Another widely used spatial light modulator (SLM), particularly in astronomy, is the deformable mirror. This is an active SLM with a reflective surface that is electrically deformed to change the wavefront shape of incident light. Deformation is achieved by moving the mirror using actuators. A large number of actuators are required for the good performance of the deformable mirror. Deformable mirrors provide a high frame rate of up to 60 kHz, which is much faster than liquid crystal (LC). The principle of aberration correction using deformable mirrors is shown in Fig.16. Two types of deformable mirrors have been developed: segmented mirrors and continuous surface mirrors. Both are shown in Fig.17, and each type will be discussed in the following paragraphs.

A segmented mirror is a simpler device that introduces phase control and modulation of light. It consists of many individual flat mirror segments of rectangular or hexagonal shape, each driven by an actuator that produces piston movement of the segment. This movement, however, only produces a stepped structure, which may not be sufficient for some applications. For better results, it is possible to add further actuators to produce tilting of the segment. However, this design is a more complex and therefore more expensive piece of equipment. Inevitably, there are some gaps between the mirror segments, causing some loss of light and diffraction losses.

The second type of deformable mirror is a continuous surface mirror. The surface can be a thin sheet of glass with a metallic or dielectric coating. Actuators apply forces to the back of the sheet to achieve the desired deformation. Fewer actuators are

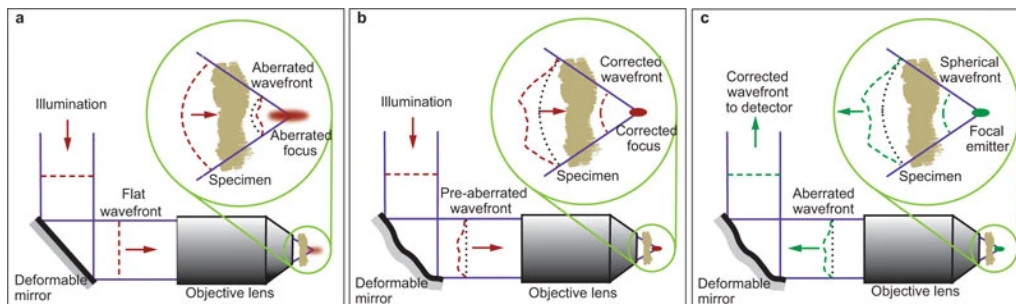


Figure 16: Principle of aberration correction in high-resolution optical microscopes. (a) Aberrations are induced as light passes through the specimen due to variations in refractive index, leading to a distortion of the focus. **(b)** The deformable mirror introduces an aberration that cancels out the specimen induced aberration, restoring a diffraction limited focus. **(c)** The deformable mirror also corrects for aberrations induced in the detection or imaging path. Adapted from [55].

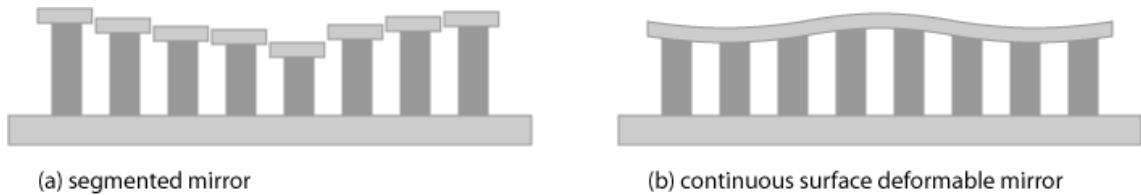


Figure 17: An illustration of two types of deformable mirror.(a) Segmented deformable mirror. (b) Continuous surface deformable mirror. Reprinted from [76].

required than with a segmented mirror because continuity is automatically ensured. Problems of light loss and diffraction are also eliminated, and a higher optical quality can be achieved. However, there may be problems with coupling between closely spaced areas.

Deformable mirror SLMs offer high frame rates, making them a good choice for adaptive optical systems in astronomy. However, they have a lower number of modulating components, resulting in lower spatial resolution.

3.2.3 Digital micromirror device

The Digital Micromirror Device (DMD) is a micro-electrical-mechanical system employed in numerous optical applications such as wave-front shaping and light focusing [77, 78]. DMS consists of a rectangular array of hundreds of thousands of individually addressable and tiltable micromirrors, each with a side length of approximately $10\ \mu\text{m}$, located on a CMOS board. Each micromirror, with its planar surfaces and high reflectivity metal coating, corresponds to a single pixel in the displayed image. The CMOS circuits provide fast and accurate control of the $+12^\circ$ or -12° tilt angle of the micromirrors, corresponding to the ON or OFF state. In the ON state, light incident on the mirror is reflected into the desired optical path, while in the OFF state, it is typically blocked, as it is reflected away from the mirror.

There are many applications in which DMD is used. It can be used in confocal microscopy, where DMD acts as a precisely controlled pinhole aperture, providing high-resolution imaging by blocking light from out-of-focus planes [79], or in structured illumination microscopy, where DMD is used for fringe projection [80]. Another useful application is the lithography of nanostructures [81].

Due to the large number of individually controlled light-modulating components, DMDs provide high spatial resolution compared to deformable mirrors. It offers frame rates of around 30 kHz, making DMD faster than LC SLM but slower than deformable mirror SLM. However, DMD only displays ON/OFF states and only allows binary amplitude modulation, as opposed to the grayscale and phase modulation possible with other SLMs [82].

3.2.4 Acousto-optic deflectors and modulators

Acousto-optic devices such as the acousto-optic deflector (AOD) or the acousto-optic modulator (AOM) are useful electrical devices used in optics. The basis of both devices is the acousto-optic effect. Both AODs and AOMs consist of a transparent crystal through which light passes. A piezoelectric transducer connected to the crystal receives a robust oscillating electrical signal from a radio frequency (RF) driver. This piezoelectric transducer induces a sound wave with a frequency typically

around 100 MHz, an acoustic wavelength in the range of 10 μm to 100 μm , and an acoustic power in the order of 1 W to 10 W. The high-power sound wave generates a propagating strain wave in the material, which, through the photoelastic effect, creates a travelling refractive index grating. This grating leads to Bragg diffraction, where the periodic variation in the refractive index affects the path of the transmitted light [83]. In the Bragg regime, phase matching of the incident and diffracted beams achieves optimum first-order diffraction and minimizes higher-order scattering. Bragg diffraction with high first-order diffraction efficiencies is commonly used in AO devices. A less commonly used diffraction regime is the Raman-Nath regime, which provides higher-order diffraction.

The AOD is used to deflect a laser beam in one direction by a variable angle. The direction of the diffracted beam is determined by a Bragg condition where the wavelength Λ and therefore the frequency f of the sound wave plays a role. The small-angle approximation holds for typical AOD diffraction, so the deflection angle, which is twice the Bragg angle $2\alpha_B$, can be calculated approximately as

$$\alpha = \frac{\lambda f}{v}, \quad (24)$$

where v is the velocity of the sound wave [84]. AODs are often used as beam scanning devices with extremely fast scanning at kilohertz rates. These scanning devices have many applications, for example in microscopy or materials processing [85]. A characteristic property of AODs is that the motion of the acoustic wave naturally introduces temporal light modulation. This effectively introduces a degree of incoherence into the diffracted light. This effect has led to AOD being used as an SLM in an artifact-free holographic light modulation (HALM) system [86]. The system consists of two AODs positioned in conjugated planes. The first, powered by complexly modulated driving signals, serves as a holographic SLM for presenting digital Fourier holograms. This SLM generates a one-dimensional target pattern in the back focal plane of a Fourier transform lens. At the same time, the second AOD, driven by sinusoidal signals, acts as a deflector to control the position of the reconstructed line. Through the synchronization of holographic diffraction and deflection, the system can generate any one- or two-dimensional pattern and may be useful device in future laser projectors and displays, structured illumination microscopy, laser material processing or optical trapping. [86]. The HALM schema is shown in Fig. 18.

AOMs are very similar to AODs, but are designed to modulate the intensity of the transmitted laser beam rather than the direction, and are referred to as intensity modulators. The power of the transmitted beam is controlled by the power of the acoustic wave. Using an AOM as an SLM could be a promising approach to generating complex spatial light modes for pulsed and short-wavelength lasers, which can damage conventional SLMs. The AOM reproduces the incident RF waveform and imprints it almost perfectly on the spatial mode of the diffracted light. The arbitrary mode can be generated by independently programmable amplitude and phase in tens of pixels. [87]. It also offers a much faster modulation pattern refresh rate than other SLMs such as DMDs or liquid crystal modulators. AOM offers mode generation switching rates of up to 500 kHz [88] and is particularly useful in applications requiring intensity modulation and dynamic control of light.

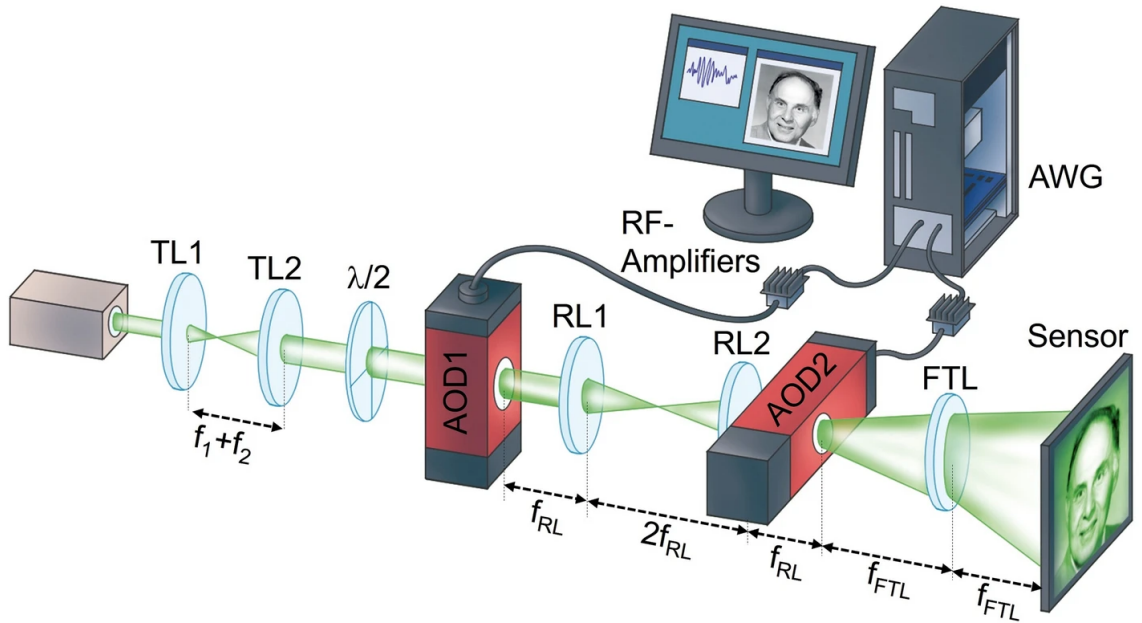


Figure 18: Conceptual setup of a holographic acousto-optic light modulation (HALM) system. A laser beam is successively modulated by a first acousto-optic deflector that displays a computer-generated hologram, and a second AOD that modulates the laser beam with a linear phase. The amplitude and phase of the hologram are computed from a digital target pattern and are encoded in the electric driving signal that controls the AOD. A lens performs an optical Fourier transform of the holographically modulated beam and reconstructs the one-dimensional target pattern that corresponds to the displayed hologram as a line in its focal plane. The position of the line is controlled through the linear phase displayed on the second AOD. The HALM system reconstructs two-dimensional patterns by sequentially reconstructing several lines at different positions. Reprinted from [86].

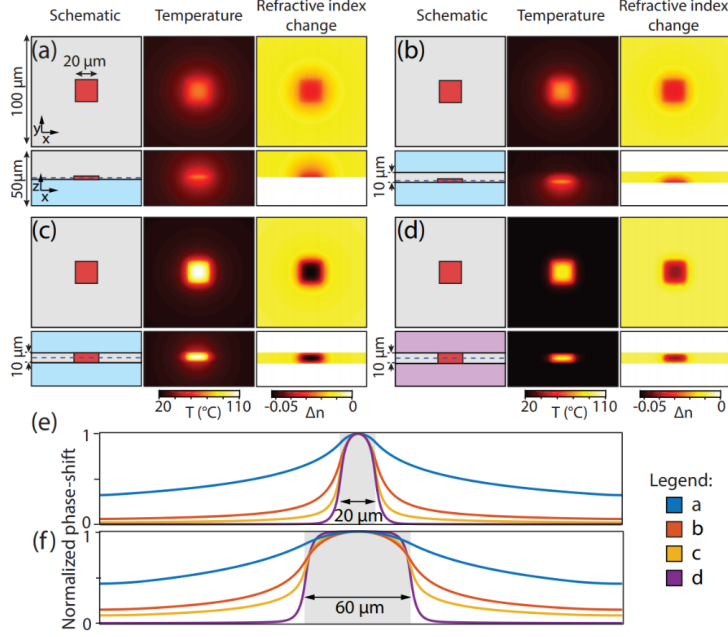


Figure 19: Numerical simulation of the temperature distribution and the refractive index change for a spatially confined heat source. (a-d) Schematics of the different simulated structures (blue=BK7, red=heat source, gray=PDMS and purple=sapphire, blue dashed lines represent the XY cross-section planes), and corresponding temperature profiles and refractive index profiles in the x,y, and x,z planes. The total power of the heat sources in each design is 2 mW. **(e)** Resulting normalized phase-shift profiles of a plane wave propagating in the z-axis direction for the four structures in (a)-(d) of 20 μm size. **(f)** The normalized phase-shift profiles considering a larger, 60 μm × 60 μm heat source in identical simulated structures (a)-(d). Reprinted from [90].

3.2.5 Photothermal spatial light modulator

Another approach to phase modulation is SLM based on the thermo-optic effect. The sensitivity of the refractive index to temperature change in some thermo-optic materials is the basis for optical phase control. When heat is applied, the refractive index changes at the point of heating, and the phase of the light wave passing through this point changes. This property of materials is quantified by the thermo-optical coefficient dn/dT . The thermo-optic effect led to the development of a photothermal SLM (PT-SLM) which is controlled by light absorption using surface plasmons resonance [89]. PT-SLM are mostly composed of optical metamaterials or metasurfaces which have received considerable attention in recent years as they allow unusual control over the phase, amplitude and polarization of light. Metasurfaces are usually formed by assembling arrays of nanoscopic light scatterers whose mutual distance is less than the wavelength. In PT-SLM, it is important to confine the refractive index change, and therefore the heat, to the area closest to the heated spot to avoid large cross-talks within the modulator. Several numerical simulations in various designs were carried out to find the best possible solution [90]. The results of the simulation are shown in Fig. 19. From these simulations, it is clear that a suitable material for encapsulating the thermo-optic material is sapphire with high thermal conductivity ($\kappa = 27.21 \text{ W m}^{-1} \text{ K}^{-1}$), which quickly dissipates heat and its temperature change is negligible.

An example of a recently introduced PT-SLM, which allows the adjustment

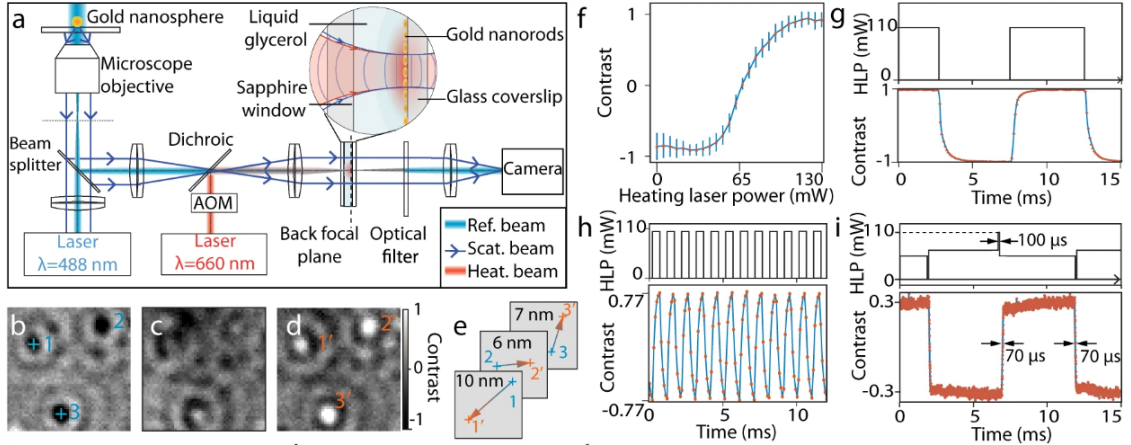


Figure 20: Experimental characterization of the PT-SLM. (a) Layout of the setup (AOM=Acousto-Optic Modulator). (b-d) Normalized iSCAT images of 30-nm single gold nanospheres at heating laser powers of (b) 0 mW, (c) 65 mW, (d) 110 mW (e) Change in the fitted position of the three nanoparticles indicated in (b) and (d). (f) Calibration curve of the particle contrast dependence on the heating power. (g) Time series of the contrast of a gold nanosphere modulated with a rectangular signal at 100 Hz (HLP Heating Laser Power) and (h) at 1 kHz. (i) Contrast time series for an arbitrary-shaped heating modulation. The upper diagram shows the corresponding temporal profile of the heating beam intensity. Reprinted from [10].

of the phase shift between the scattered light and the reference beam in iSCAT microscopy, is presented in the study by H.M.L. Robert et al. [10]. The PT-SLM used consisted of a layer of gold nanorods in liquid glycerol attached to a glass coverslip on one side and a sapphire window on the other. Liquid glycerol was used as the thermo-optic material with a large negative thermo-optic coefficient. $dn/dT = -2.7 \times 10^{-4} K^{-1}$, which is >10 times higher than the substrate (glass) and the superstrate (sapphire). The well-chosen medium and substrates allowed for a strong temperature gradient and a limited refractive index gradient within the thermo-optic material. The PT-SLM achieved a phase switching time of $70 \mu s$, which is two orders of magnitude faster than conventional liquid crystal devices. The modulator also exhibits phase stability in the milliradian range [10]. The experimental characterisation of PT-SLM is shown in Fig. 20.

3.3 Influence of subnanometre surface roughness on interference contrast

In microscopic methods such as fluorescence microscopy, surface roughness does not play a significant role. However, the highly sensitive iSCAT has shown that even sub-nanometre surface roughness can cause noticeable speckle patterns [91]. The detection of stationary nanoscopic scatterers on the substrate remains a challenge, even though they are clearly visible under an AFM. Undulations on the sub-nanometre scale exhibit a non-uniform distribution, with certain domains exhibiting an abundance of peaks or dips, forming laterally extending 'hill' or 'valley' domains spanning hundreds of nanometres. At these lateral scales, the hill or valley domains can effectively act as scattering volumes similar to 10-20 nm diameter gold nanoparticles,

leading to interference contrasts of comparable magnitude. As a result, there is a lower size limit for the scatterers than would theoretically apply to observations on a perfectly flat surface. In the recent publication [91], the experimental data are showing that the difference in phase patterns is induced by subtle variations in the roughness of the substrate. The roughness of the substrate forms a kind of fingerprint that is always specific to a particular area of the surface. This problem is illustrated in Fig.21. The measured contrast in Fig.21b varies even though the size of the gold nanoparticles (GNPs) is the same according to the AFM measurement shown in Fig.21c. The contrast distribution is then much broader than for an ideally flat surface, as can be seen in Fig.21d. However, the surface fingerprints have potential applications for lateral position and displacement sensing with angstrom level precision. The accurate marker-free substrate positioning and full recovery of the measured speckle pattern, as illustrated in Fig.21, enabled the identification and localization of nanoscopic features immobilized on the surface, even during processes performed outside the microscope (e.g., spin-coating of nanoparticles onto the glass coverslip). This capability could be of great benefit in super-resolution imaging or in the semiconductor industry for nanofabrication[91].

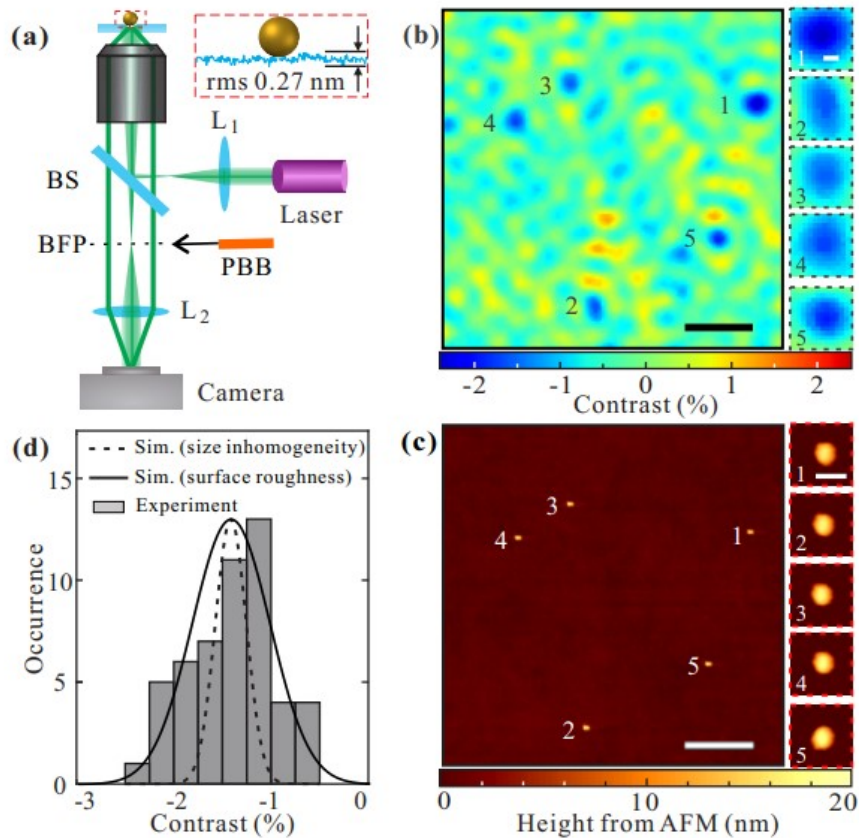


Figure 21: The effect of surface roughness of coverslip on particle contrast. (a) Schematic of the experimental setup and the sample consisting of individual GNPs on a glass coverslip. A partial beam block (PBB) could be inserted to the back-focal plane (BFP). (b) Interference contrast image of the sample. Signals of the GNPs are labeled and enlarged on the right side. (c) AFM topographic image of the same area of (b). Zoomed-in images of the GNPs are given on the right. (d) A histogram of the interference contrasts measured from 52 GNPs on the same coverslip. The dashed and solid lines are the simulated distributions for GNPs on a perfectly flat coverslip and on the coverslip with surface roughness considered, respectively. Scale bars: $1\ \mu\text{m}$ (black), $100\ \text{nm}$ (white). Reprinted from [91].

4. Experimental part

The experimental part focuses on the development of a new generation of PT-SLM elements, their characterisation and proof-of-concept implementation in an ultrasensitive quantitative phase imaging setup. The phase imaging experiment also aims to support the theoretical model of surface fingerprints discussed in the previous section. The first subsection describes the specific details of the operation of the PT-SLM used in the experiments in the context of the previously published designs. It also provides details of the experimental structure preparation, aiming for future investigation and optimization of the PT-SLM for promising applications. The second subsection provides details of the characterisation of the performance of the newly manufactured PT-SLM. Finally, the third section outlines the experimental setup for quantitative phase detection and describes the experiment aimed at detecting the scattering amplitude and phase of a sample. Specifically, it focuses on gold nanoparticles on two different surfaces, with the aim of comparing the effect of surface roughness on the measured phase.

4.1 Photothermal spatial light modulator development

4.1.1 Description of photothermal spatial light modulator

This subsection deals with the description of PT-SLM samples prepared and characterized in a previous publication [90]. The PT-SLM consists of a thin layer of the thermo-optic material polydimethylsiloxane (PDMS) elastomer. This material has a high linear negative thermo-optical coefficient, with a value of $dn/dT = -4.5 \times 10^{-4} K^{-1}$. The PDMS is doped with gold nanoparticles (GNPs) that are uniformly distributed throughout the material, effectively acting as a distributed heat source. The PT-SLM has an absorbance peak around the excitation wavelength of 532 nm, and the mean diameter size of the GNPs was calculated to be 48 ± 2 nm [90]. The thermo-optic layer is surrounded on both sides by a transparent material, such as glass or sapphire. This transparent material acts as a heat sink. The thermal conductivity of (borosilicate crown) glass and sapphire is $1.13 \text{ Wm}^{-1}\text{K}^{-1}$ and $27.21 \text{ Wm}^{-1}\text{K}^{-1}$, respectively. The scheme and photos of PT-SLM are shown in Fig.22.

4.1.2 The working principle of the photothermal spatial light modulator

The operating principle of the PT-SLM is based on the photothermal effect as described in section 3.2.5. Here it is explained how the PT-SLM can be used

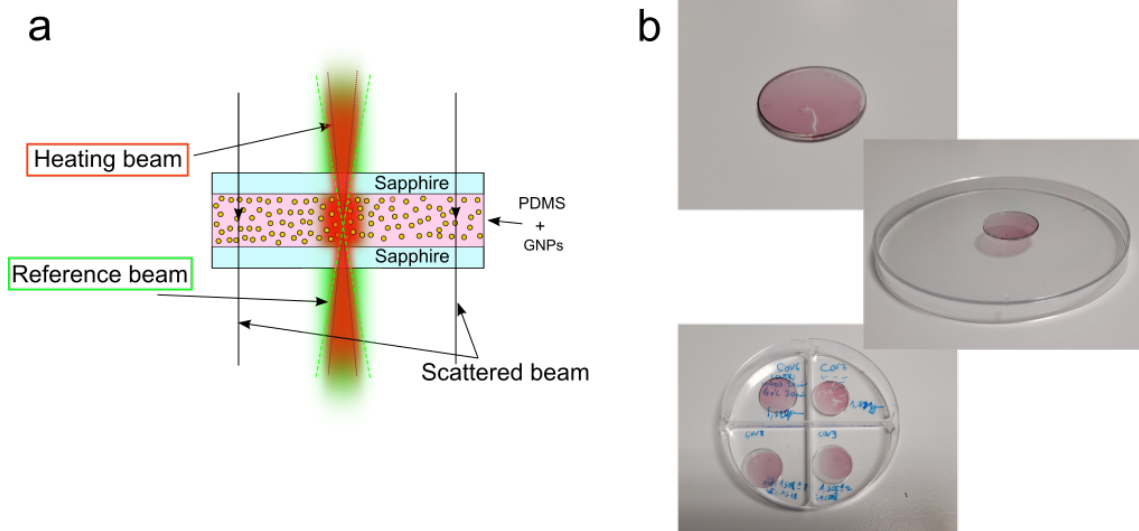


Figure 22: PT-SLM used in experiment. (a) Scheme of PT-SLM. The heating beam (here marked in red) is absorbed by the GNPs and causes the PDMS layer to heat up, thus changing the refractive index. The reference beam (here marked in green), which passes through the same spot, senses the refractive index change and the response is in the form of a change in propagation speed. (b) Photos of PT-SLM used in the experiment.

in iSCAT for the phase delay between the reference and the scattered light. The PT-SLM is positioned in the back focal plane of the microscope objective, where the phase delay between the reference and signal beams can be modulated. In this configuration, the reference beam is focused on the thermal heating spot while the signal beam propagates in parallel further away from the heated spot. Simulations and subsequent measurements of the light intensity distribution in the back focal plane were carried out in [92] and are shown in Fig. 23. The bright spot in the red dashed circle in the centre represents the contribution of the reference beam and the part outside the circle represents the scattered beam. As the reference beam is focused on the heating spot, its velocity changes due to variations in the refractive index of the medium ($c = c_0/n$). This results in a relative phase delay compared to the unfocused scattered beam, where the effect of the refractive index change is practically negligible ($<0.25\%$) [10]. The PT-SLM thus allows the image contrast to be varied by changing the temperature at the focal point, and the equation is then supplemented by a new term

$$c = \frac{2E_s}{E_r} \cos(\Delta\phi + \phi(T)). \quad (25)$$

4.1.3 Manufacture of photothermal spatial light modulator

The protocol for the synthesis of the GNPs in the PDMS medium was adapted from [93]. PDMS elastomer kits (Sylgard 184, Dow Corning) containing PDMS base and the curing agent were used to prepare the PDMS medium. The curing agent cross-links the elastomer and causes it to cure. Gold(III) chloride trihydrate (Sigma–Aldrich) was used for the synthesis of GNPs. First, the Au(III) chloride trihydrate powder (9 mg) was mechanically mixed with the PDMS base (2.43 g in mass ratio of 3.7[mg]:1[g]). Then it was sonicated for one hour at 37 kHz at a temperature of 60°C. After sonication bath the PDMS curing agent (221 mg) was added to the

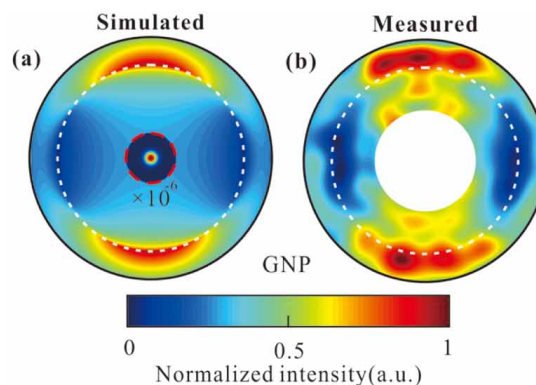


Figure 23: The light intensity distribution in the BFP. (a) The light intensity at the BFP calculated for a 40 nm GNP on a mica surface under the normal illumination of a Gaussian beam from the mica surface. The intensity within the red-dashed circle is multiplied by 10^{-6} . (b) The measured BFP pattern for the scattered field from a 100 nm GNP. The white area of the image corresponds to the part for blocking the reference beam in the experiment. Reprinted from [92]

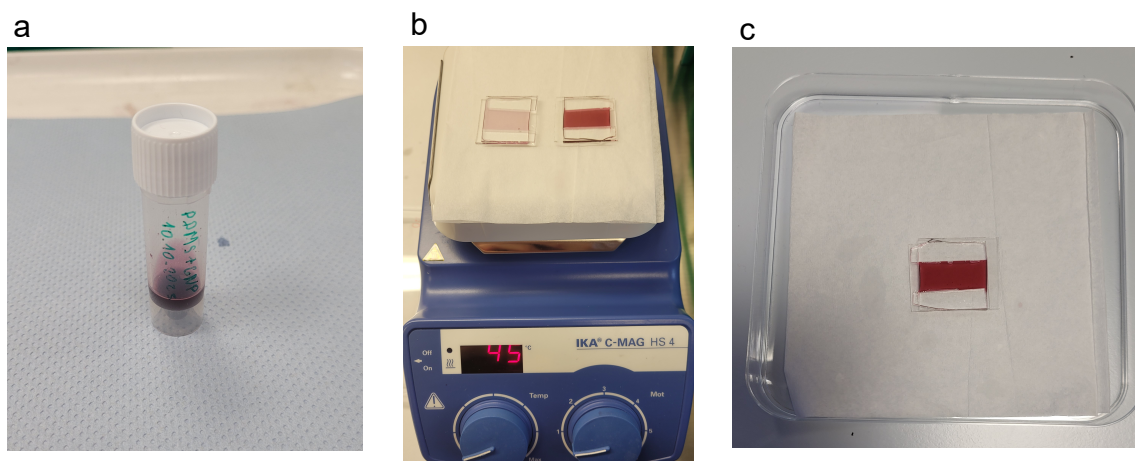


Figure 24: New sample of PT-SLM. (a) Tube with liquid sample with formed gold nanoparticles. (b) The heating plate with samples. (c) Finished solidified sample.

mixture and mechanically mixed. The final mixture was degassed under vacuum for 10 minutes to remove the air bubbles. Finally it was sonicated for 30 minutes at 37 kHz at about 10°C. The final concentration of GNPs can be reduced by adding mixture of PDMS base and PDMS curing agent. The mixture was stored in the refrigerator. The tube containing the liquid sample is shown in the Fig. 24a.

To encapsulate the PDMS with GNPs, a glass sheet was cut into equal-sized squares. The glass squares were cleaned in isopropyl alcohol in an ultrasonic bath. In addition, two glass rectangles were cut and glued between the two glass squares using optical adhesive to form a 1 mm thick channel. The PDMS mixture with GNPs was pipetted onto the glass and moved within the channel by capillary force. The sample was left in this form in a refrigerator for 2 days to remove any remaining small air bubbles. The sample was then placed on a heating plate and left for 7 days at 45°C to allow the solution to solidify. The solidification process and the resulting sample are shown in Fig. 24b,c.

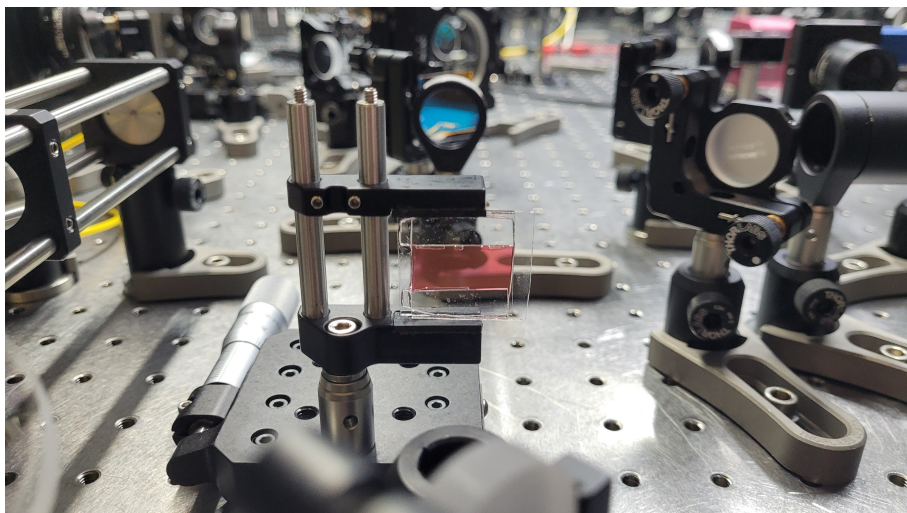


Figure 25: Linear translation stage with Pt-SLM.

4.2 Characterisation of photothermal spatial light modulator

A new setup was built to characterise PT-SLM. The setup was used to measure spatial resolution and response time. Two acousto-optical deflectors (AODs) are positioned one behind the other. Both AODs are connected to amplitude and frequency signals, and one- or two-dimensional images are programmed using Arduino software. The heating beam, responsible for inducing temperature changes in the PT-SLM, enters the AODs arrangement and the required image is displayed on the PT-SLM via two lenses and a dichroic mirror. The PT-SLM is positioned in the focal plane of the lens. A He-Ne laser beam with a wavelength of 632 nm is directed from the other side of the PT-SLM and has a beam diameter of 1.5 cm in the plane in which the PT-SLM is located and completely surrounds the image projected onto the PT-SLM by the heating beam. The stage with the PT-SLM is shown in Fig. 25.

4.2.1 Spatial resolution of photothermal spatial light modulator

The off-axis digital holography configuration was set up to characterise the spatial resolution. A portion of the imaging light was separated by a beam splitter to construct the reference arm. The light path length of the reference arm was aligned by a linear translation stage to ensure the same light path length for both the reference and imaging arms. The reference and imaging light paths were joined by a second beam splitter and interfered with each other on the camera. The setup for off-axis digital holography is shown in Fig. 26A. The interference fringes produced by unmodulated light are shown in Fig. 26B. After modulating the phase of the imaging beam by the image sent to the PT-SLM, the interference pattern appeared on the camera, as shown in Fig. 26C. The calculated phase is shown in Fig. 26D. To set the spatial resolution limit, two points were sent from the AODs to the PT-SLM, decreasing the distance between them until two points could be distinguished in the computed phase image.

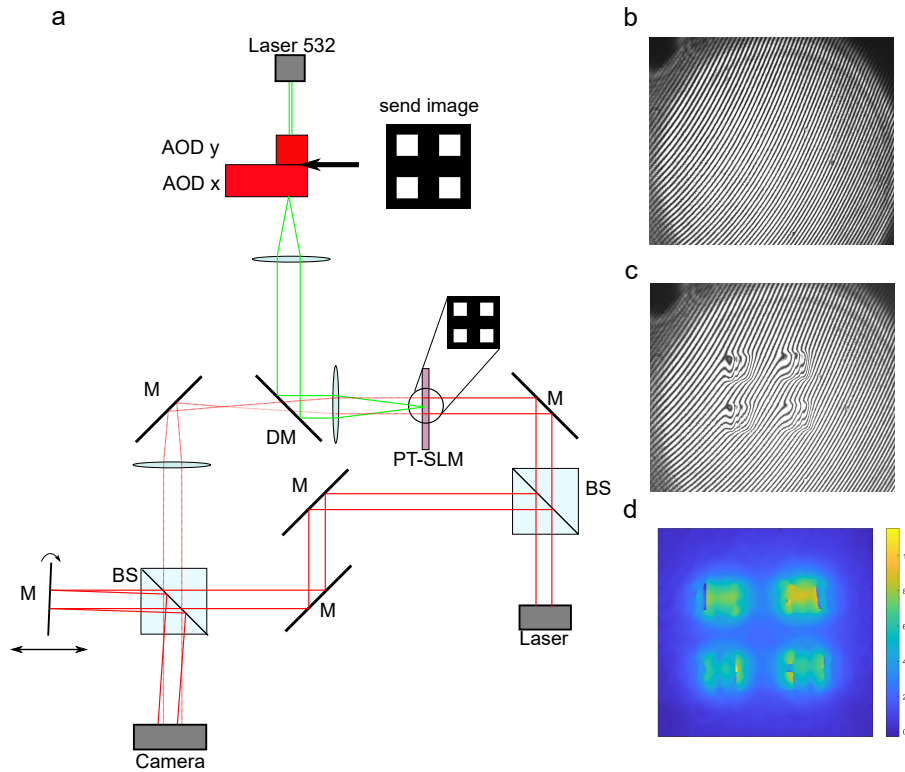


Figure 26: PT-SLM characterisation. (a) The setup for measuring the spatial resolution of the PT-SLM. The reference arm provides an off-axis configuration to construct a digital holography method for phase measurement. (b) **Image of background** First the image of background was taken. (c) **Image of phase change** Image sent from AODs and displayed on the PT-SLM caused the phase change in the wavefront of the imaging beam. (d) **The computed phase.**

4.2.2 Response time of photothermal spatial light modulator

A similar setup was used to measure the response time of the PT-SLM, but without the reference arm and beam splitter. The imaging beam was limited by the aperture and a lens was added to position the camera in the focal plane of the PT-SLM. The AODs were first configured to completely block the heating light beam, resulting in the signal image being centred on the camera with no phase shift. A signal was then sent to the AODs to allow the full heating beam to pass through at maximum laser power (2W). As the AODs allowed the heating beam to pass, the signal image on the camera shifted laterally due to the changing phase of the imaging light. After a few seconds, the AODs were adjusted to block the heating beam again, causing the signal image on the camera to return to the centre.

4.2.3 Absorbance measurement

The NanoDrop One UV/Vis spectrophotometer was used to measure the absorbance peak of the solution of PDMS and GNPs. The concentration of GNPs had to be reduced to maximise the transparency of the sample in order to obtain quality results. A small amount of the sample was added to the cuvette that can be placed in the instrument.

4.3 Phase detection of gold nanoparticles

4.3.1 Sample preparation

Glass coverslips were first cleaned of dust particles using nitrogen gas. They were then chemically cleaned using acetone in the first step and Milli-Q water in the second step in an ultrasonic cleaner. For the second surface, the very thin layer of mica was cleaved from the mica circular disc. The thin layer was glued to one of the cleaned glass coverslips using optical adhesive (an adhesive with minimal effect on light propagation) and placed in a box with UV light to solidify the adhesive. A solution containing 30-nm gold nanoparticles (GNP) (2×10^{11} particles per ml and with average size 28 - 32 nm) was then spin-coated on clean glass coverslip and freshly cleaved mica (at a maximum speed of 100 rotations per second) to ensure uniform distribution of the nanoparticles on the surface.

4.3.2 Surface roughness measurement

In order to compare the surface roughness of the glass coverslip and the mica, both were measured using the NanoWizard3 atomic force microscope (JPK instruments AG). The size of the measured area was $4 \times 4 \mu\text{m}$ (or 512×512 pixels). The tapping mode of the measurement had speed was $25 \mu\text{m/s}$ and the duration of one field of view (FOV) was 2.4 ms. The resolution of the AFM NanoWizard3 is less than 0.035 nm. The canteliver had the spring constant 3 N/m and the frequency 75 kHz. The silicon canteliver was $225 \mu\text{m}$ long and $35 \mu\text{m}$ wide and the tip had a radius 8 nm.

4.3.3 Experiment procedure and setup

The sample was placed above the microscope objective with numeric aperture $\text{NA} = 1.45$ on the 3-axis piezo sample stage. The sample was illuminated through a microscope objective by a collimated beam of continuous single-frequency diode-pumped laser (Cobolt Jive) operating at $\lambda = 561 \text{ nm}$. Part of the beam was reflected from the glass-air interface to form a reference beam. The rest of the beam passed through, and a fraction of it is scattered on the sample. Both reflected and scattered beams were directed through the microscope objective and beam splitter into the 4f system, where the Fourier plane is accessible. Here in the back focal plane of the microscope objective, the PT-SLM was placed. In this experiment the PT-SLM with thickness of $95 \mu\text{m}$ enclosed by sapphire was used. A heating solid-state continuous single transverse mode green laser with a wavelength of 532 nm (Quantum gem) is guided into the optical path through a dichroic mirror and is focused on the back focal plane of the microscope objective, which is also the Fourier plane of the 4f system. The heating beam has a diameter of $60 \mu\text{m}$ at the focus and overlaps the reference beam in order to enable phase shifting. Since the heating laser is continuous, it was necessary to implement an acousto-optic modulator to modulate the intensity. A CMOS camera (Photonfocus) was placed behind the 4f system to acquire the resulting interference image. The photos of the experimental setup are shown in Fig. 27.

A LabVIEW program was employed to automatise the overall measurement. The piezo stage, AOM and camera were integrated into the program. For each surface

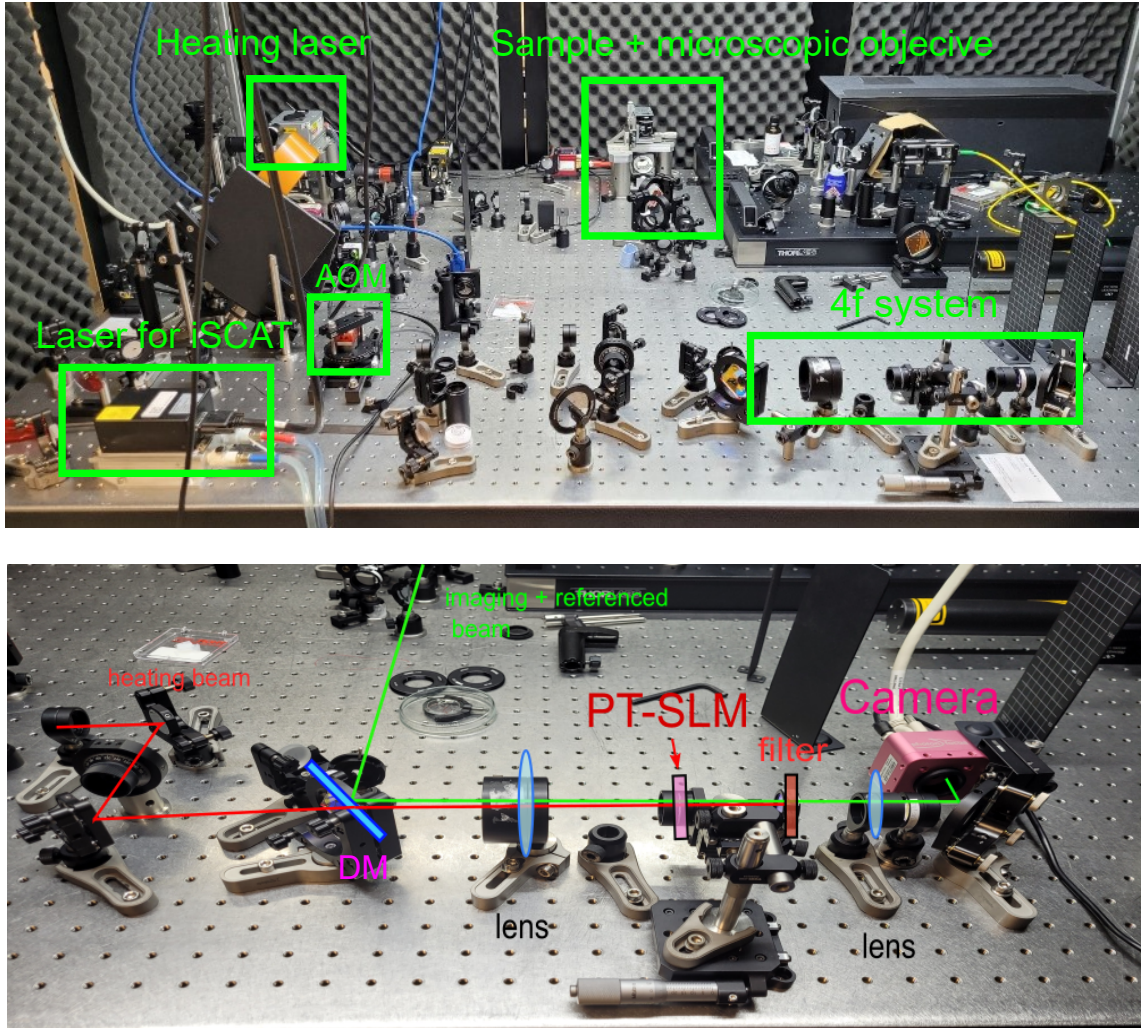


Figure 27: Experimental setup. Top photo. The layout of the lasers and sample stage on the optical table. In the lower right corner is the 4f system. It also shows the location of the acousto-optic modulator AOM in the optical path of the heating laser. **Bottom photo.** Detail of 4f system. The dichroic mirror (DM) allows the heating laser beam to follow the same optical path as the reference and scattered beam. The two lenses form a 4f system where a PT-SLM on a linear translation stage is placed in the Fourier plane. In addition, there is a filter that does not allow the heating beam to fall onto the camera.

measurement, the piezo stage performed scans over 256 fields of view (FOV). Within each FOV, 250 images were acquired with different heating powers applied by the AOM laser intensity modulation. One field of view is of the size of $4.5 \times 4.5 \mu\text{m}$.

As many FOVs were measured, it was necessary to incorporate an autofocus system (Kinesis K-Cube Position Sensing Detector) to ensure that the microscope objective remained in the correct focus position throughout the scan.

5. Results

5.1 Characterization of photothermal spatial light modulator

The spatial resolution of the new PT-SLM element was measured in the digital holography setup described in section 4.2.2. The interference fringes were recorded by the camera. The transmitted image changed the phase of the imaging light, leading to a change in the interference image. The recorded image was processed with Fast Fourier Transform in 2D (fft2 function in MATLAB). The phase image was obtained by calculating the angle and subtracting the angle value from the background to show only the phase change. The resulting phase image is in Fig. 28. Fig. 28 (a) is a phase image of two points 14 pixels apart, corresponding to $470\ \mu\text{m}$. In Fig. 28 (b) is the cross section of the phase image in the line of the points. In Fig. 28 (c) and (e) are the points with mutual distance 8 pixels and 4 pixels which correspond to $268\ \mu\text{m}$ and $134\ \mu\text{m}$ respectively. Figures (d) and (f) in Fig. 28 show the corresponding cross sections. The spatial resolution limit is around $250\ \mu\text{m}$ when we use a laser power of around $100\ \text{mW}$.

The chessboard pattern with $44\times 44\ \mu\text{m}$ square cell was projected onto the PT-SLM from the publication [10]. The obtained phase image was well resolved for samples with thickness $95\ \mu\text{m}$, $31\ \mu\text{m}$ and $22\ \mu\text{m}$ and lower limit for spatial resolution was assumed but not provided.

To measure the response and cooling (recovery) time signal at maximum laser power, the phase of the imaging beam was changed and the phase change was recorded by the camera in the focal plane of the PT-SLM. The response and cooling times were derived from the 10% to 90% phase change. The time response of the phase shift is in Fig. 29. The response time of the new PT-SLM sample is 6 s.

The response time of the sample fabricated in publication [90] was characterised by using that fast camera in the image plane where the framerate used was 20 kHz. Squared-shaped phase-shifts were projected on the PT-SLM and the response time was obtained from the intensity change captured on the fast camera. The sample with thickness of $95\ \mu\text{m}$ had response time 9 ms and the sample with thickness $22\ \mu\text{m}$ had response time 0.7 ms [10].

The longer response time compared to the PT-SLM introduced in publication [90] is due to the significantly higher layer thickness (x10). Another reason could be the different concentration of GNPs. The long cooling time, calculated as 10 s, is also due to the thickness, but also to the fact that the new PT-SLM is encased in glass, which has a lower thermal conductivity than the previously used sapphire. This results in slower heat transfer from the PDMS.

The absorbance peak of the new sample was around $530\ \text{nm}$ which corresponds to the measurement in [90]. The measured absorbance peak is shown in Fig. 30.

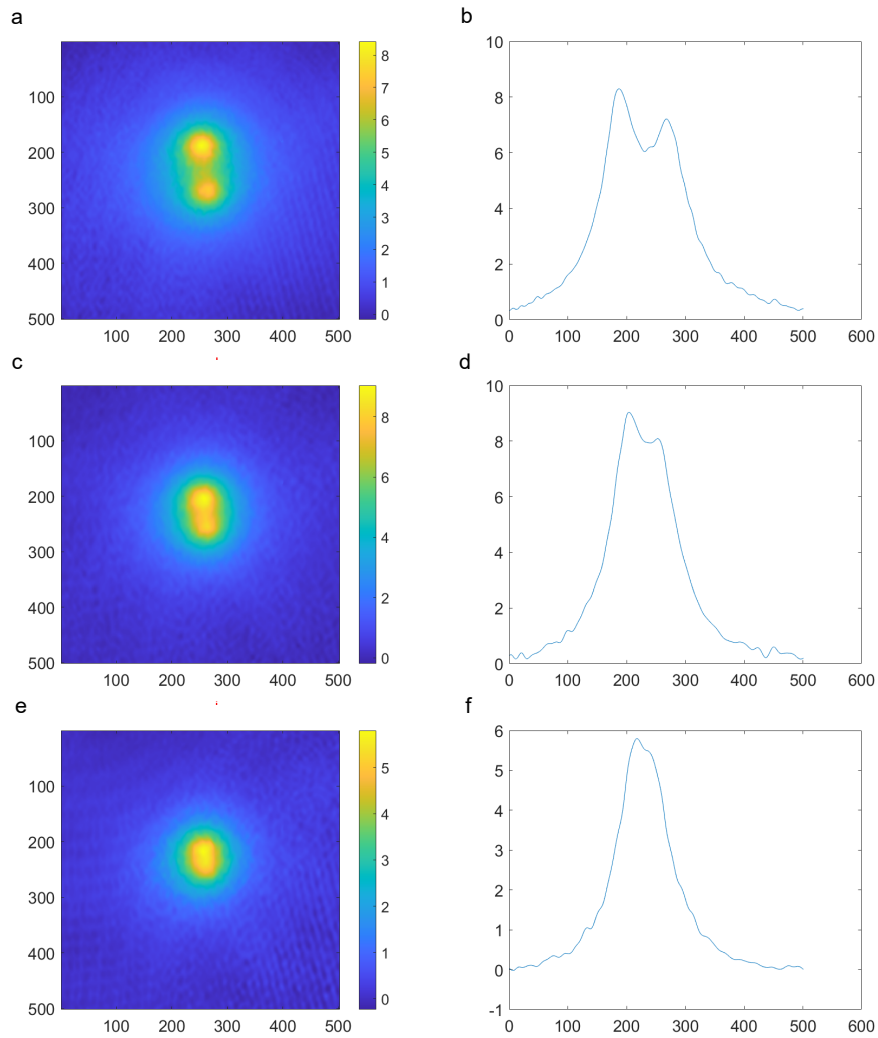


Figure 28: Spatial resolution. measured with digital holography setup. The distance between two points is $470\ \mu\text{m}$ (a), $268\ \mu\text{m}$ (c) and $134\ \mu\text{m}$ (e), respectively. (b, d, f) The corresponding cross-section over the phase image.

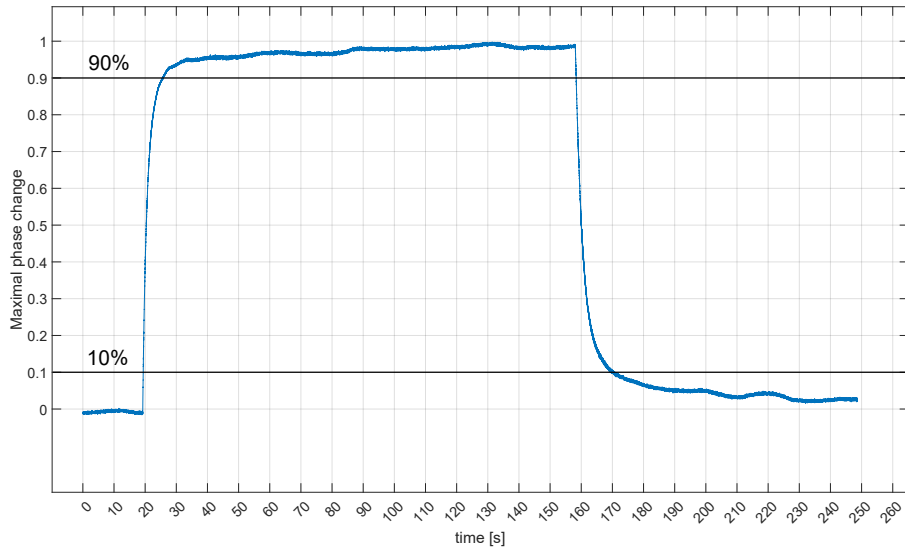


Figure 29: Respons and cooling time. The plot of the time response of the phase shift after applying the maximum heating power.

These results mean that using the laser with a wavelength of 532 nm as the heating laser was a good choice.

5.2 Phase detection of gold nanoparticles

Following the previous experimental study by the group described in 3.3, we explore the effect of the near-field coupling between the surface undulations and the scattering amplitude of single gold nanoparticles. Figure 21C indicates that surface roughness significantly affects the homogeneity of the detected scattering contrast of nanoparticles deposited on the rough surface, and we hypothesise that this effect derives predominantly from the particle-to-particle variation of the scattering phase. Therefore, we performed quantitative phase imaging on a set of nanoparticles deposited on a glass surface and on a surface of atomically flat mica and compared the distribution of the scattering phase versus the scattering amplitude.

The results of the AFM measurement are shown in Fig. 31. It is noticeable that the surface of the glass coverslip has more irregularities, creating maps of peaks and valleys. In contrast, the mica is uniform with no major irregularities. The root mean square (RMS) of the profile height deviations for mica for this sample is stable around 230 pm, whereas for glass it varies from 300 to 400 pm depending on the position of the line from which the RMS is calculated.

With the use of a heating laser and an AOM, it was possible to modulate the phase. With the maximum laser power 2 W, 2π modulation was obtained for the sample with 30-nm GNPs. Firstly, a 128x128 pixel FOV for 250 different laser powers, i.e. for 250 different phase shifts. 256 FOVs were scanned in this way and the entire modulation of the laser power for all FOVs, which is $5184\mu\text{m}^2$, took approximately 10 hours. The measured contrast values at the position with the GNP were modulated sinusoidally with increasing laser power. The laser power was increased so that at least 2π modulation occurred. The modulation curve of the contrast values and the corresponding phase shift are shown in Fig. 32. From the

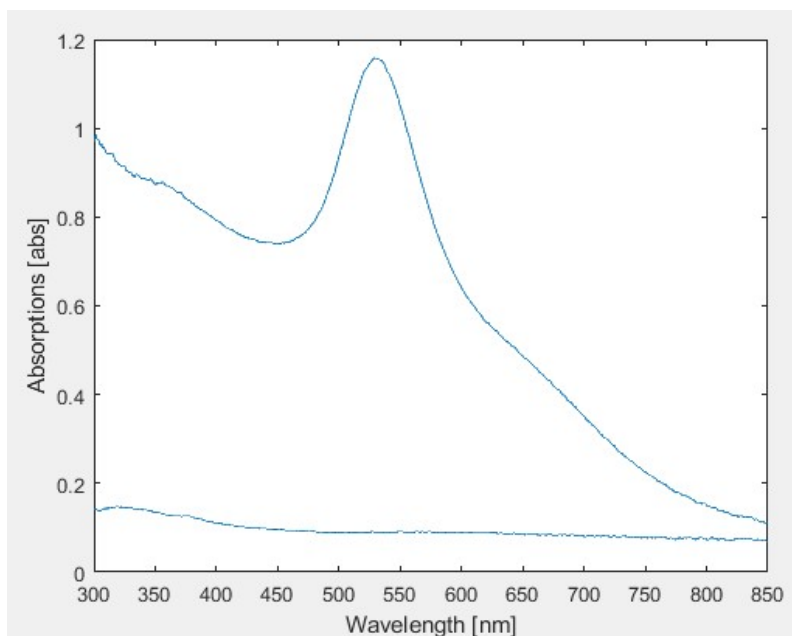


Figure 30: Absorbance peak. measured in spectrophotometer. The peak corresponds to wavelength around 530 nm.

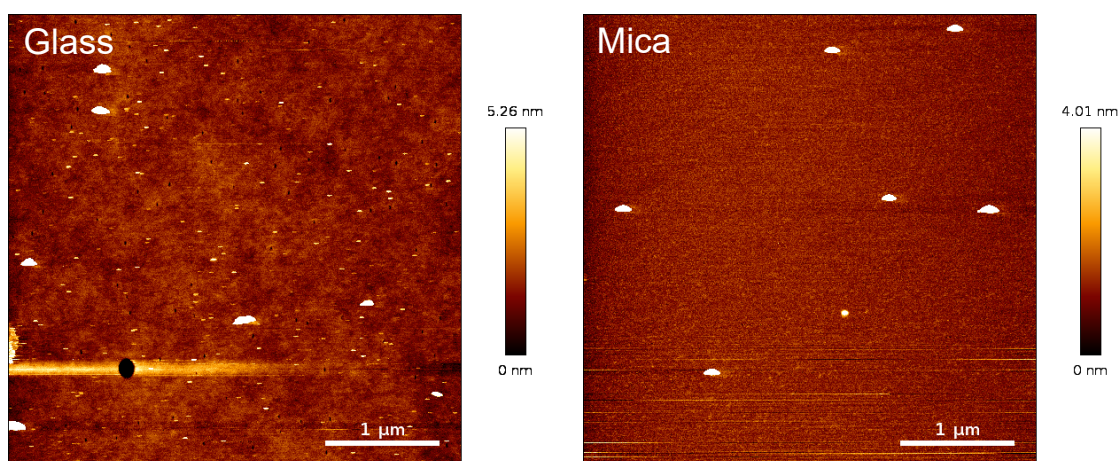


Figure 31: AFM measurement. Glass and mica surface measured by atomic force microscopy. White larger dots represent the 30 nm GNPs. They are not included in the color bar here.

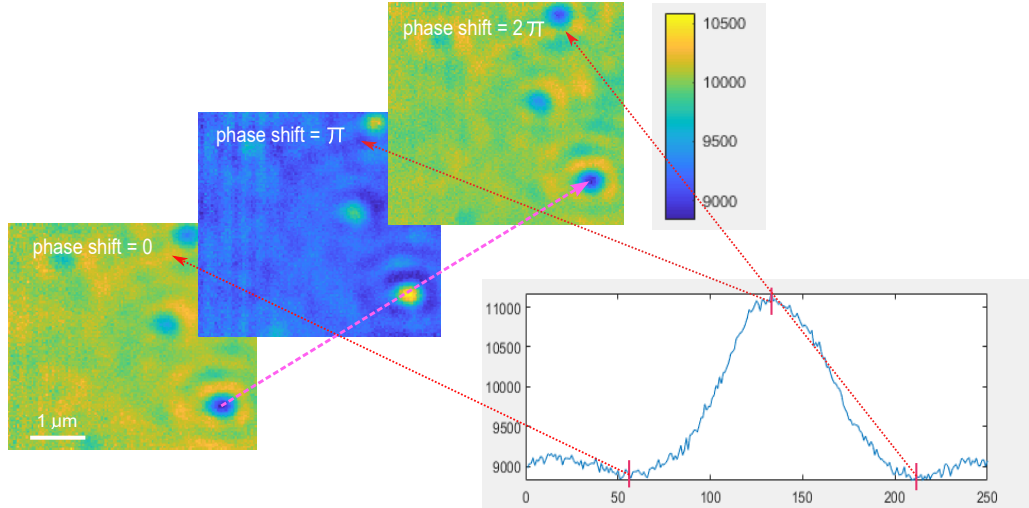


Figure 32: Phase shift induced by heating beam. Phase shift 0π , π and 2π . The phase follows the sine curve.

measured data, it was observed that the first few values were almost invariant. This could be due to non-linear characteristics of the AOM modulation on the laser power. This part was not useful for the phase calculation and was therefore excluded from the calculations. The remaining values were used to calculate the Fourier transform

$$FT = \sum_{m=0}^{n-1} y e^{-i2\pi m/p}, \quad (26)$$

where y is the contrast value, n is the number of different laser power steps and p is the period, i.e. number of steps in one period. The amplitude and phase are then calculated as

$$\text{amp} = |FT| \quad (27)$$

$$\text{phase} = \text{angle}(FT). \quad (28)$$

By modulating the laser power and thus the phase shift, it was possible to calculate the phase of the GNPs. The whole procedure was performed for GNPs on glass coverslips and on mica. The results of the contrast measurement and the calculated phase are shown in Fig. 33. The contrast measurement shows that GNPs on glass coverslips have a different contrast distribution compared to GNPs measured on mica, where they all have very similar contrast. The same results can be seen from the calculated phase, where there is a significant difference between the phase values for GNPs on glass.

The phase, amplitude, and iSCAT contrast in the histograms in Fig. 34 (a, b) are collected from all detected GNPs measured on glass and mica. As there is a certain distribution in the size of the GNPs leading to different amplitude values, nanoparticles with the same measured amplitude were selected to compare contrast and phase values of nanoparticles of the same size. In Fig. 34 (c, d) the values have been filtered for the GNPs with the most represented amplitude (within a small range). The wider distribution of the phase is well shown in the scatter plots in Fig. 34 (e, f). The variance of the filtered phase values is 1.24 for glass and 0.37 for mica.

The plots of the contrast values and the corresponding phase for the glass and mica surfaces are shown in Fig. 35. The plots in Fig. 35 (a,b) show data for all

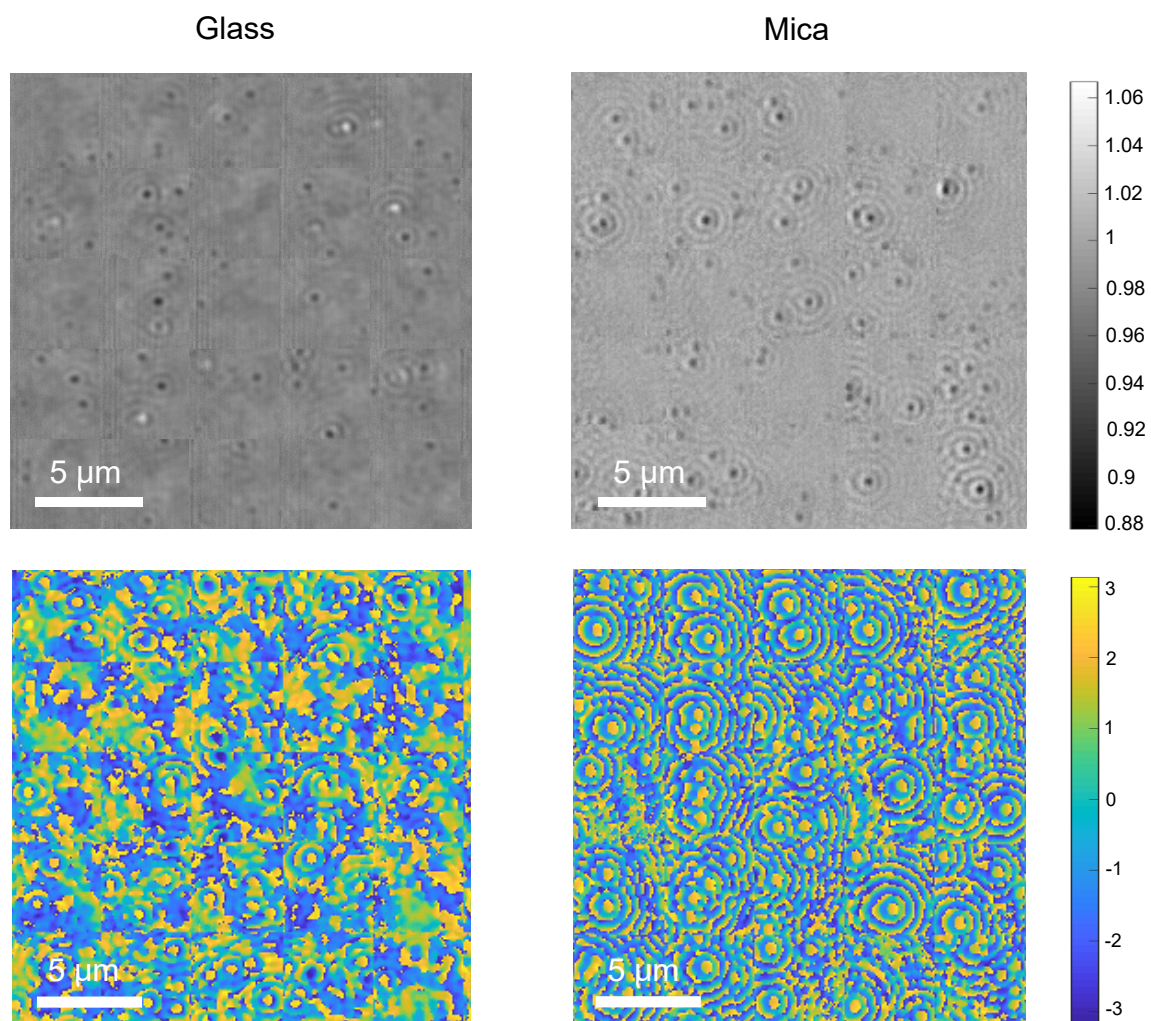


Figure 33: Contrast and phase. Measured iSCAT contrast and calculated phase map of the sample with GNPs on glass and mica.

measured GNPs. It is clear that the contrast is much more uniform for the mica than for the glass coverslip. What changes significantly is the amplitude more than the phase shift. On the other hand, the contrast measured on glass suffers from more obvious phase shifts. In Fig. 35 (c,d) the plots show the data for nanoparticles of the same size (i.e., amplitude). Again, the contrast measured on the glass coverslip has a broader distribution than that measured on the mica.

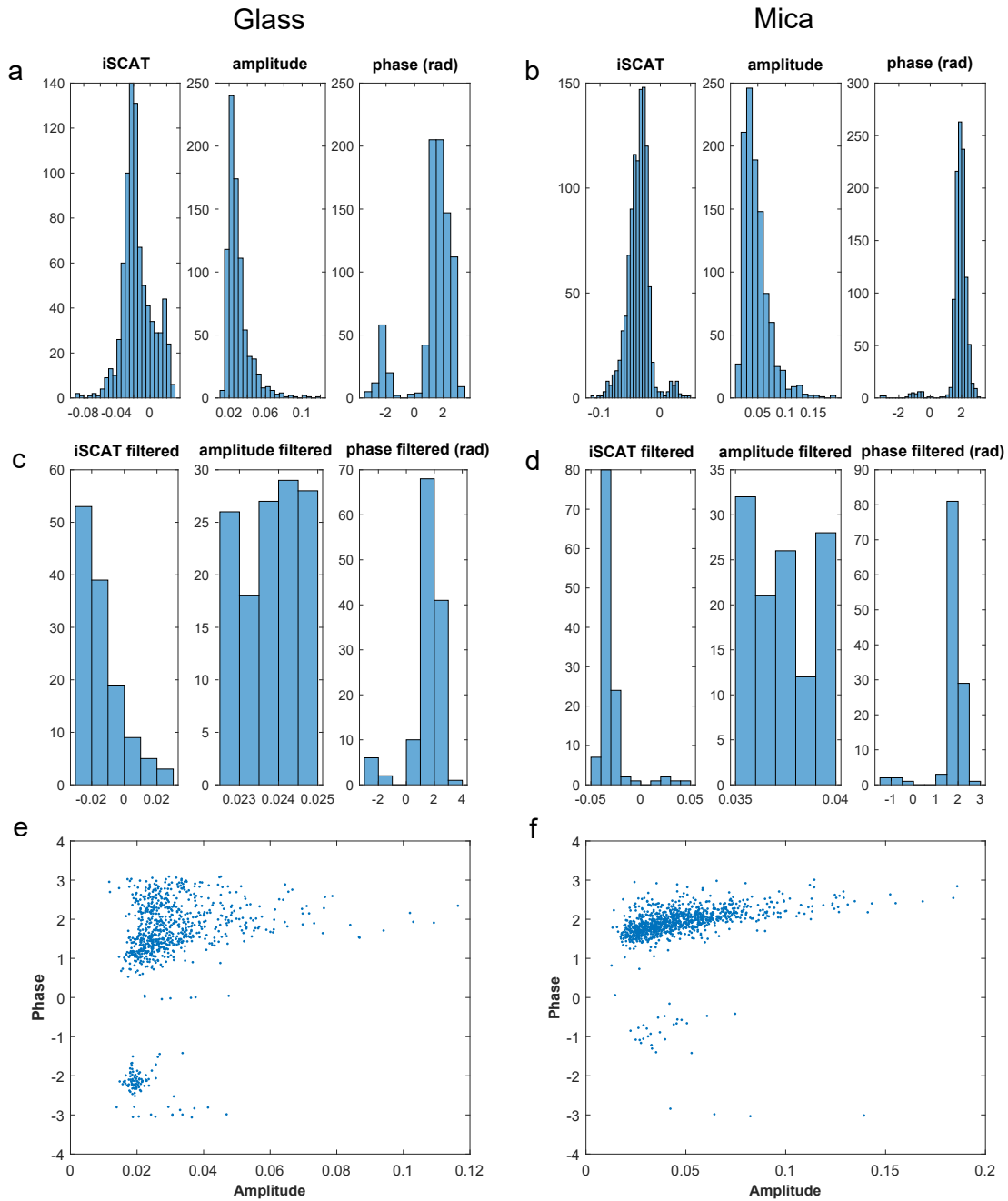


Figure 34: iSCAT contrast, amplitude and phase histograms. Histograms with measured values of iSCAT contrast, amplitude and phase for glass (a) and mica (b). (c, d) Filtered values for nanoparticles with the most amplitude representation. (e, f) Scattered plot of phase values with all detected nanoparticles.

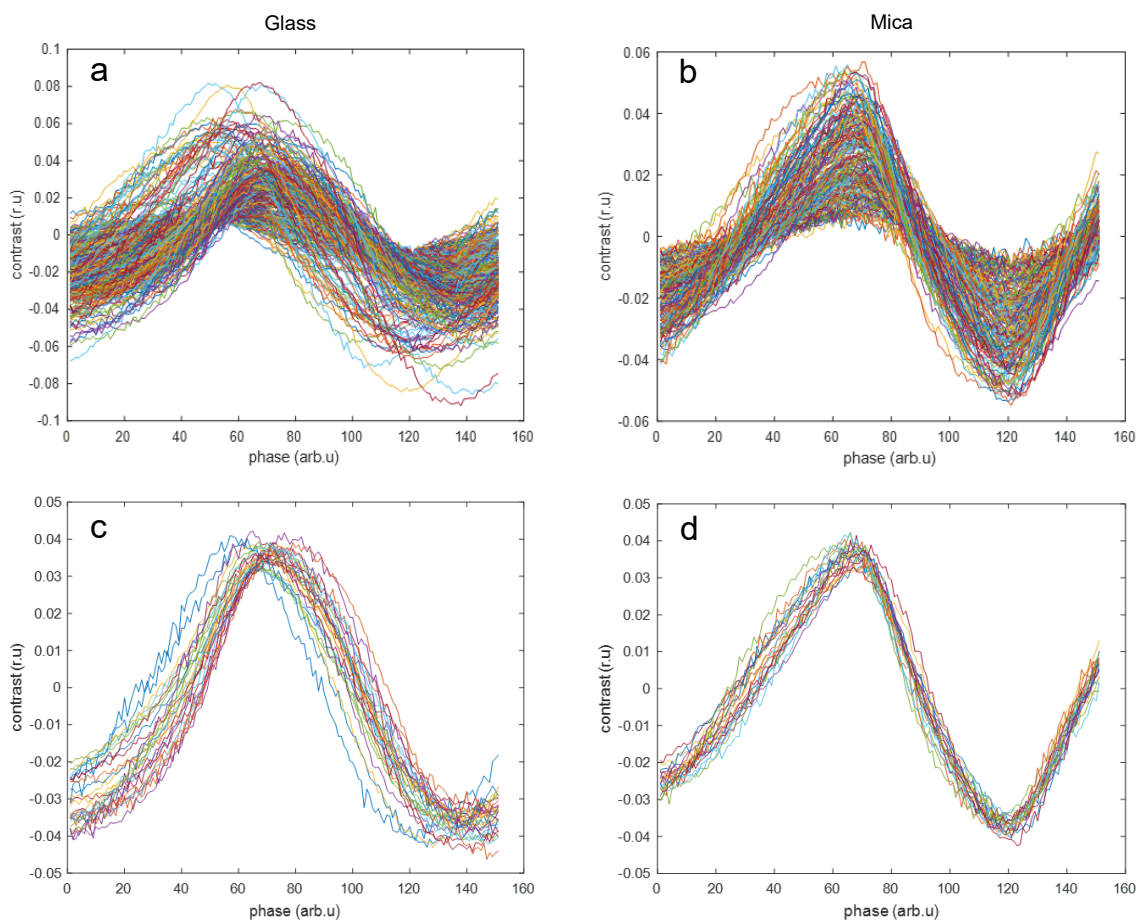


Figure 35: Contrast plots with phase shift. Measured contrast values versus phase for glass (a, c) and mica (b, d). (a,b) Values for all measured particles. (c, d) Values for selected nanoparticles with the same amplitude.

Discussion and conclusion

This thesis provides a comprehensive review of microscopy methods, including fluorescence microscopy, interferometric scattering microscopy, and mass photometry, with particular emphasis on the critical role of phase information in single-molecule imaging. The introduction of quantitative phase imaging and the detailed exploration of interferometric methods such as single-molecule localisation microscopy, digital holography microscopy, and wavefront sensing methods mark significant advancements in the field. The review further extended into closely related techniques of adaptive optics, highlighting innovations in spatial light modulators, in particular liquid crystals and deformable mirrors, and delved into the intricate details of photothermal spatial light modulators (PT-SLMs), highlighting the previous artwork this thesis builds upon. An important discussion was also presented on the influence of sub-nanometre surface roughness on interference contrast, which is a key aspect in nanoscopy, yet weakly understood.

The experimental section of this thesis is divided into three distinct parts. Firstly, the structure and operating principles of the PT-SLM were outlined, including a thorough protocol for its fabrication. A significant improvement over the previous generation, which relied on liquid glycerol, is the use of solid PDMS material with a higher thermo-optic coefficient. The challenges in the manufacturing process include maintaining precision in the proportions of PDMS and Au(III) chloride trihydrate powder and ensuring the same parameters during the nanoparticle formation process to achieve uniformity of size and concentration. The pursuit of an effective and reproducible manufacturing process remains ongoing, with the introduction of sapphire substrates instead of glass expected to bring a significant improvement.

In the second experimental phase, the focus shifted to characterising the functionality of the PT-SLM. Measurements of spatial resolution and response time revealed significant deviations from previous studies, attributed to the increased thickness of the thermo-optic layer. This is an important and expected performance trade-off for increasing the modulated field of view and needs to be considered for future developments. These findings pave the way for further characterisation and optimisation of the PT-SLM, which holds great promise in adaptive optics applications, including the correction of atmospheric aberrations and the development of smart lenses capable of multi-plane focusing, which would go far beyond the scope of this thesis.

The culmination of this research was the novel integration of interferometric scattering microscopy with PT-SLM to develop a ground-breaking quantitative phase imaging method. The experiment successfully demonstrated the ability to induce phase shifts between reflected and scattered light by heating the PT-SLM. The phase extraction of 30nm gold nanoparticles, achieved through a Fourier transform

analysis of their contrast changes, revealed distinct phase characteristics between different surfaces. This crucial finding not only confirms recent publications, but also highlights the improved precision and statistical relevance of far-field optical responses to sub-nanometre non-resonant dielectric features.

Looking ahead, there is a clear path for further exploration and refinement in the field of ultrasensitive phase detection nanoscopy. Further development and optimisation of PT-SLM technology, particularly in terms of material composition and layer thickness, will be essential. In addition, the potential applications of this technology in adaptive optics, in particular atmospheric aberration correction and advanced imaging techniques, provide exciting alternative paths for research. The integration of PT-SLM into various microscopy techniques and its impact on enhancing image resolution and contrast warrant deeper investigation. Furthermore, the extension of the experimental datasets and the employment of the developed methodologies on a wider range of nanoscopic elements can significantly contribute to the understanding of their optical properties.

In conclusion, this thesis not only reviews the current state of microscopy techniques and phase detection in nanoscopy, but also introduces innovative approaches and experimental findings that push the boundaries of ultrasensitive quantitative phase imaging. The insights gained from our studies are invaluable in advancing the understanding and application of ultrasensitive nanoscopy and provide a foundation for future research and technological development in this rapidly evolving field.

References

1. WEISENBURGER, S.; SANDOGHDAR, V. Light microscopy: an ongoing contemporary revolution. *Contemporary Physics*. 2015, vol. 56, pp. 123–143. Available from DOI: 10.1080/00107514.2015.1026557.
2. HELL, S. W.; WICHMANN, J. Breaking the diffraction resolution limit by stimulated emission: stimulated-emission-depletion fluorescence microscopy. *Opt. Lett.* 1994, vol. 19, pp. 780–782. Available from DOI: 10.1364/OL.19.000780.
3. GUSTAFSSON, M. G. L. Nonlinear structured-illumination microscopy: Wide-field fluorescence imaging with theoretically unlimited resolution. *Proceedings of the National Academy of Sciences*. 2005, vol. 102, pp. 13081–13086. Available from DOI: 10.1073/pnas.0406877102.
4. LELEK, M.; GYPARAKI, M. T.; BELIU, G.; SCHUEDER, F.; GRIFFIÉ, J.; MANLEY, S.; JUNGSMANN, R.; SAUER, M.; LAKADAMYALI, M.; ZIMMER, C. Single-molecule localization microscopy. *Nature Reviews Methods Primers*. 2021, vol. 1. Available from DOI: 10.1038/s43586-021-00038-x.
5. SIGAL, Y. M.; ZHOU, R.; ZHUANG, X. Visualizing and discovering cellular structures with super-resolution microscopy. *Science*. 2018, vol. 361, pp. 880–887. Available from DOI: 10.1126/science.aau1044.
6. MAGIDSON, V.; KHODJAKOV, A. Chapter 23 - Circumventing Photodamage in Live-Cell Microscopy. In: *Digital Microscopy*. Academic Press, 2013, vol. 114, pp. 545–560. ISSN 0091-679X. Available from DOI: <https://doi.org/10.1016/B978-0-12-407761-4.00023-3>.
7. V.ASTRATOV. *Label-Free Super-Resolution Microscopy*. Springer Cham, 2019.
8. PILIARIK, M.; SANDOGHDAR, V. Direct optical sensing of single unlabelled proteins and super-resolution imaging of their binding sites. *Nature Communications*. 2014, vol. 5. Available from DOI: 10.1038/ncomms5495.
9. YOUNG, G.; HUNDT, N.; COLE, D. et al. Quantitative mass imaging of single biological macromolecules. *Science*. 2018, vol. 360, pp. 423–427. Available from DOI: 10.1126/science.aar5839.
10. ROBERT, H. M. L.; HOLANOVÁ, K.; BUJAK, L.; VALA, M.; HENRICHS, V.; LÁNSKÝ, Z.; PILIARIK, M. Fast photothermal spatial light modulation for quantitative phase imaging at the nanoscale. *Nature Communications*. 2021, vol. 12. Available from DOI: 10.1038/s41467-021-23252-3.
11. HUANG, B.; BATES, M.; ZHUANG, X. Super-resolution fluorescence microscopy. *Annu Rev Biochem*. 2009, vol. 78, pp. 993–1016. Available from DOI: 10.1146/annurev.biochem.77.061906.092014.
12. ABBE, E. Beiträge zur Theorie des Mikroskops und der mikroskopischen Wahrnehmung. *Archiv für mikroskopische Anatomie*. 1873, vol. IX.

13. RAYLEIGH. Investigations in optics, with special reference to the spectro-scope. *London, Edinburgh, and Dublin Philosophical Magazine and Journal of Science*. 1879, vol. 8.
14. SPARROW, M. On spectroscopic resolving power. *Astrophysical Journal*. 1916, vol. 44.
15. BORN, M.; WOLF, E. *Principles of Optics*. Pergamon, Oxford, 1980.
16. UTAH—ADVANCED MICROSCOPY, The University of. *Super-Resolution Microscopy Tutorial [Online]*, Accessed: 2023. 2011. Available also from: <https://advanced-microscopy.utah.edu/education/super-res/>.
17. *The Nobel Prize in Chemistry 2023*. 2023-11. Available also from: <https://www.nobelprize.org/prizes/chemistry/2023/summary/>.
18. EFROS, A. L.; BRUS, L. E. Nanocrystal Quantum Dots: From Discovery to Modern Development. *ACS Nano*. 2021, vol. 15, no. 4, pp. 6192–6210. Available from DOI: 10.1021/acsnano.1c01399.
19. KORTAN, A. R.; HULL, R.; OPILA, R. L.; BAWENDI, M. G.; STEIGERWALD, M. L.; CARROLL, P. J.; BRUS, Louis E. Nucleation and Growth of CdSe on ZnS Quantum Crystallite Seeds, and Vice Versa, in Inverse Micelle Media. *Journal of the American Chemical Society*. 1990, vol. 112, no. 4, pp. 1327–1332. Available from DOI: 10.1021/ja00160a005.
20. EKIMOV, A.I.; EFROS, A.L.; ONUSHCHENKO, A.A. Quantum size effect in semiconductor microcrystals. *Solid State Communications*. 1985, vol. 56, no. 11, pp. 921–924. ISSN 0038-1098. Available from DOI: [https://doi.org/10.1016/S0038-1098\(85\)80025-9](https://doi.org/10.1016/S0038-1098(85)80025-9).
21. TSOI, K. M.; DAI, Q.; ALMAN, B. A.; CHAN, W. C. W. Are Quantum Dots Toxic? Exploring the Discrepancy Between Cell Culture and Animal Studies. *Accounts of Chemical Research*. 2013, vol. 46, pp. 662–671. Available from DOI: 10.1021/ar300040z.
22. CHIBLI, H.; CARLINI, L.; PARK, S.; DIMITRIJEVIC, N. M.; NADEAU, J. L. Cytotoxicity of InP/ZnS quantum dots related to reactive oxygen species generation. *Nanoscale*. 2011, vol. 3, pp. 2552–2559. Available from DOI: 10.1039/C1NR10131E.
23. CHOU, L. Y. T.; CHAN, W. C. W. A strategy to assemble nanoparticles with polymers for mitigating cytotoxicity and enabling size tuning. *Nanomedicine*. 2011, vol. 6, pp. 767–775. Available from DOI: 10.2217/nnm.11.58.
24. GÖTTFERT, F.; WURM, C. A.; MUELLER, V.; BERNING, S.; CORDES, V. C.; HONIGMANN, A.; HELL, S. W. Coaligned dual-channel STED nanoscopy and molecular diffusion analysis at 20 nm resolution. *Biophys J*. 2013. Available from DOI: [doi:10.1016/j.bpj](https://doi.org/10.1016/j.bpj).
25. HEIN, B.; WILLIG, K. I.; HELL, S. W. Stimulated emission depletion (STED) nanoscopy of a fluorescent protein-labeled organelle inside a living cell. *Proceedings of the National Academy of Sciences*. 2008, vol. 105, no. 38, pp. 14271–14276. Available from DOI: 10.1073/pnas.0807705105.
26. LINDFORS, K.; KALKBRENNER, T.; STOLLER, P.; SANDOGHDAR, V. Detection and Spectroscopy of Gold Nanoparticles Using Supercontinuum White Light Confocal Microscopy. *Phys. Rev. Lett*. 2004, vol. 93. Available from DOI: 10.1103/PhysRevLett.93.037401.
27. TAYLOR, R.; SANDOGHDAR, V. Interferometric scattering microscopy: Seeing single nanoparticles and molecules via Rayleigh scattering. *Nano Lett*. 2019,

- vol. 19, pp. 4827–4835. Available from DOI: <https://doi.org/10.1021/acs.nanolett.9b01822>.
28. BOHREN, C.F.; HUFFMAN, D.R. *Absorption and Scattering of Light by Small Particles*. John Wiley and Sons, 1983. ISBN 978-0-471-29340-8.
 29. PRIEST, L.; PETERS, J. S.; KUKURA, P. Scattering-based Light Microscopy: From Metal Nanoparticles to Single Proteins. *Chemical Reviews*. 2021, vol. 121, no. 19, pp. 11937–11970. Available from DOI: <https://doi.org/10.1021/acs.chemrev.1c00271>.
 30. ASTRATOV, V. (ed.). *Label-Free Super-Resolution Microscopy*. Springer, 2019. ISBN 9783030217228. Available from DOI: <https://doi.org/10.1007/978-3-030-21722-8>.
 31. GEMEINHARDT, A.; MCDONALD, M. P.; KÖNIG, K.; AIGNER, M.; MACKENSEN, A.; SANDOGHDAR, V. Label-Free Imaging of Single Proteins Secreted from Living Cells via iSCAT Microscopy. *J. Vis. Exp.* 2018, vol. 141. Available from DOI: [10.3791/58486](https://doi.org/10.3791/58486).
 32. SPINDLER, S.; EHRIG, J.; KÖNIG, K.; NOWAK, T.; PILIARIK, M.; STEIN, H. E.; TAYLOR, R. W.; GARANGER, E.; LECOMMANDOUX, S.; ALVES, I. D.; SANDOGHDAR, V. Visualization of lipids and proteins at high spatial and temporal resolution via interferometric scattering (iSCAT) microscopy. *Journal of Physics D: Applied Physics*. 2016, vol. 49, no. 27. Available from DOI: [10.1088/0022-3727/49/27/274002](https://doi.org/10.1088/0022-3727/49/27/274002).
 33. WIT, Ga. de; ALBRECHT, D.; EWERS, H.; KUKURA, P. Revealing Compartmentalized Diffusion in Living Cells with Interferometric Scattering Microscopy. *Biophysical Journal*. 2018, vol. 114, pp. 2945–2950. Available from DOI: <https://doi.org/10.1016/j.bpj.2018.05.007>.
 34. KÜPPERS, M.; ALBRECHT, D.; KASHKANNOVA, A. D.; LÜHR, J.; SANDOGHDAR, V. Confocal interferometric scattering microscopy reveals 3D nanoscopic structure and dynamics in live cells. *Nature Communications*. 2023, vol. 14. Available from DOI: [10.1038/s41467-023-37497-7](https://doi.org/10.1038/s41467-023-37497-7).
 35. HSIAO, Yi-Teng; WU, Tsai-Ying; WU, Bo-Kuan; CHU, Shi-Wei; HSIEH, Chia-Lung. Spinning disk interferometric scattering confocal microscopy captures millisecond timescale dynamics of living cells. *Opt. Express*. 2022, vol. 30, no. 25, pp. 45233–45245. Available from DOI: [10.1364/OE.471935](https://doi.org/10.1364/OE.471935).
 36. BECKER, J.; PETERS, J. S.; CROOKS, I.; HELMI, S.; SYNAKEWICZ, M.; SCHULER, B.; KUKURA, P. A Quantitative Description for Optical Mass Measurement of Single Biomolecules. *ACS Photonics*. 2023, vol. 10, no. 8, pp. 2699–2710. Available from DOI: [10.1021/acsphotonics.3c00422](https://doi.org/10.1021/acsphotonics.3c00422).
 37. FOLEY, E. D. B.; KUSHWAH, M. S.; YOUNG, G.; KUKURA, P. Mass photometry enables label-free tracking and mass measurement of single proteins on lipid bilayers. *Nature Methods*. 2021, vol. 18, pp. 1247–1252. Available from DOI: [10.1038/s41592-021-01261-w](https://doi.org/10.1038/s41592-021-01261-w).
 38. ZERNIKE, F. Phase contrast, a new method for the microscopic observation of transparent objects part II. *Physica*. 1942, vol. 9, pp. 974–986. Available from DOI: [https://doi.org/10.1016/S0031-8914\(42\)80079-8](https://doi.org/10.1016/S0031-8914(42)80079-8).
 39. POPESCU, G. *Quantitative Phase Imaging of Cells and Tissues, 1st ed.* New York: McGraw-Hill, 2011. ISBN 9780071663427.
 40. NGUYEN, T. L.; PRADEEP, S.; JUDSON-TORRES, R. L.; REED, J.; TEITELL, M. A.; ZANGLE, T. A. Quantitative Phase Imaging: Recent Advances

- and Expanding Potential in Biomedicine. *ACS Nano*. 2022, vol. 16, no. 8, pp. 11516–11544. Available from DOI: doi:10.1021/acsnano.1c11507.
41. MIR, M.; BHADURI, B.; WANG, Ru; ZHU, R.; POPESCU, G. Chapter 3 - Quantitative Phase Imaging. In: WOLF, E. (ed.). *Progress in Optics*. Elsevier, 2012, vol. 57, pp. 133–217. ISSN 0079-6638. Available from DOI: <https://doi.org/10.1016/B978-0-44-459422-8.00003-5>.
 42. HU, C.; POPESCU, G. Physical significance of backscattering phase measurements. *Opt. Lett.* 2017, vol. 42, pp. 4643–4646. Available from DOI: <https://doi.org/10.1364/OL.42.004643>.
 43. PARK, Y.; DEPEURSINGE, C.; POPESCU, G. Quantitative phase imaging in biomedicine. *Nature Photonics*. 2018, vol. 12, pp. 578–589. Available from DOI: <https://doi.org/10.1038/s41566-018-0253-x>.
 44. WANG, Zhuo.; MILLET, L.; MIR, M.; DING, H.; UNARUNOTAI, S.; ROGERS, J.; GILLETTE, M. U.; POPESCU, G. Spatial light interference microscopy (SLIM). *Opt. Express*. [N.d.], vol. 19, pp. 1016–1026. Available from DOI: 10.1364/OE.19.001016.
 45. WANG, Zhuo; CHUN, Ik Su; LI, Xiuling; ONG, Zhun-Yong; POP, Eric; MILLET, Larry; GILLETTE, Martha; POPESCU, Gabriel. Topography and refractometry of nanostructures using spatial light interference microscopy. *Opt. Lett.* 2010, vol. 35, pp. 208–210. Available from DOI: 10.1364/OL.35.000208.
 46. PHAM, H.; DING, H.; SOBH, N.; DO, M.; PATEL, S.; POPESCU, G. Off-axis quantitative phase imaging processing using CUDA: toward real-time applications. *Biomed. Opt. Express*. 2011, vol. 2, pp. 1781–1793. Available from DOI: 10.1364/BOE.2.001781.
 47. MARQUET, P.; RAPPAZ, B.; MAGISTRETTI, P. J.; CUCHE, E.; EMERY, Y.; COLOMB, T.; DEPEURSINGE, Ch. Digital holographic microscopy: a noninvasive contrast imaging technique allowing quantitative visualization of living cells with subwavelength axial accuracy. *Opt. Lett.* 2005, vol. 30, no. 5, pp. 468–470. Available from DOI: 10.1364/OL.30.000468.
 48. TIKEDA; POPESCU, G.; DASARI, R. R.; FELD, M. S. Hilbert phase microscopy for investigating fast dynamics in transparent systems. *Opt. Lett.* 2005, vol. 30, no. 10, pp. 1165–1167. Available from DOI: 10.1364/OL.30.001165.
 49. ZHANG, T.; IYAMAGUCHI. Three-dimensional microscopy with phase-shifting digital holography. *Opt. Lett.* 1998, vol. 23, no. 15, pp. 1221–1223. Available from DOI: 10.1364/OL.23.001221.
 50. ZHANG, Q.; HU, Q.; BERLAGE, C.; KNER, P.; JUDKEWITZ, B.; BOOTH, M.; JI, N. Adaptive optics for optical microscopy. *Biomed Opt Express*. 2023, vol. 14, no. 4, pp. 1732–1756. Available from DOI: 10.1364/BOE.479886.
 51. SHACK, R. B; PLATT, B. C. Production and use of a lenticular Hartmann screen. *J. Opt. Soc. Am.* 1971, vol. 16.
 52. PLATT, B. C.; SHACK, R. History and Principles of Shack-Hartmann Wavefront Sensing. *Journal of Refractive Surgery*. 2001, vol. 17, no. 5, S573–S577. Available from DOI: 10.3928/1081-597X-20010901-13.
 53. BON, P.; MAUCORT, G.; WATTELLIER, B.; MONNERET, S. Quadriwave lateral shearing interferometry for quantitative phase microscopy of living cells. *Opt. Express*. 2009, vol. 17, no. 15, pp. 13080–13094. Available from DOI: 10.1364/OE.17.013080.

54. RAGAZZONI, R. Pupil plane wavefront sensing with an oscillating prism. *Journal of Modern Optics*. 1996, vol. 43, no. 2, pp. 289–293. Available from DOI: 10.1080/09500349608232742.
55. BOOTH, M. J. Adaptive optical microscopy: the ongoing quest for a perfect image. *Light: Science Applications*. 2014, vol. 3. Available from DOI: 10.1038/lssa.2014.46.
56. NEIL, M. A. A.; BOOTH, M. J.; WILSON, T. New modal wave-front sensor: a theoretical analysis. *J. Opt. Soc. Am. A*. 2000, vol. 17, no. 6, pp. 1098–1107. Available from DOI: 10.1364/JOSAA.17.001098.
57. BECKERS, J. M. Adaptive optics for astronomy: principles, performance, and applications. *Annu. Rev. Astron. Astr.* 1996, vol. 31, pp. 13–62. Available from DOI: 10.1146/annurev.aa.31.090193.000305.
58. MADEC, P.-Y. Overview of deformable mirror technologies for adaptive optics and astronomy. In: ELLERBROEK, Brent L.; MARCHETTI, Enrico; VÉRAN, Jean-Pierre (eds.). *Adaptive Optics Systems III*. SPIE, International Society for Optics and Photonics, 2012, vol. 8447, pp. 22–39. Available from DOI: 10.1117/12.924892.
59. BOOTH, M. J.; NEIL, M. A.; JUSKAITIS, R.; WILSON, T. Adaptive aberration correction in a confocal microscope. *Proc Natl Acad Sci U S A*. 2002, vol. 99. Available from DOI: 10.1073/pnas.082544799.
60. RUECKEL, N.; MACK-BUCHER, J. A.; DENK, W. Adaptive wavefront correction in two-photon microscopy using coherence-gated wavefront sensing. *Proc Natl Acad Sci U S A*. 2006, vol. 103. Available from DOI: 10.1073/pnas.0604791103.
61. RODRÍGUEZ, C.; JI, Na. Adaptive optical microscopy for neurobiology. *Current Opinion in Neurobiology*. 2018, vol. 50, pp. 83–91. ISSN 0959-4388. Available from DOI: <https://doi.org/10.1016/j.conb.2018.01.011>.
62. HAMPSON, K. M.; TURCOTTE, R.; MILLER, D. T.; KUROKAWA, K.; MALES, J. R.; JI, Na; BOOTH, M. J. Adaptive optics for high-resolution imaging. *Nature Reviews Methods Primers*. 2021, vol. 1. Available from DOI: 10.1038/s43586-021-00066-7.
63. CHA, Jae-Won; BALLESTA, J.; SO, P. T. C. Shack-Hartmann wavefront-sensor-based adaptive optics system for multiphoton microscopy. *Journal of Biomedical Optics*. 2010, vol. 15, no. 4. Available from DOI: 10.1117/1.3475954.
64. MAURER, C.; JESACHER, A.; BERNET, S.; RITSCH-MARTE, M. What spatial light modulators can do for optical microscopy. *Laser Photon. Rev.* 2011, vol. 5, pp. 81–101. Available from DOI: 10.1002/lpor.200900047.
65. KÜHN, J. G.; JOLISSAINT, L.; BOUXIN, A.; PATAPIS, P. SLM-based active focal-plane coronagraphy: status and future on-sky prospects. 2021, vol. 11451, pp. 378–386. Available from DOI: 10.1117/12.2562579.
66. TAKAKI, Yasuhiro; OKADA, Naoya. Hologram generation by horizontal scanning of a high-speed spatial light modulator. *Appl. Opt.* 2009, vol. 48, pp. 3255–3260. Available from DOI: 10.1364/AO.48.003255.
67. HONGXIN, Z.; JIAN, Z.; LIYING, W. Evaluation of phase-only liquid crystal spatial light modulator for phase modulation performance using a Twyman–Green interferometer. *Measurement Science and Technology*. 2007, vol. 18, pp. 1724–1728. Available from DOI: 10.1088/0957-0233/18/6/s09.

68. HORNBECK, L. J. Deformable-Mirror Spatial Light Modulators. *SPIE*. 1990, vol. 1150, pp. 86–103. Available from DOI: 10.1117/12.962188.
69. WATTS, C.M.; SHREKENHAMER, D.; MONTOYA, J.; LIPWORTH, G.; HUNT, J.; SLEASMAN, T.; KRISHNA, S.; SMITH, D. R.; PADILLA, W. J. Terahertz compressive imaging with metamaterial spatial light modulators. *Nature Photonics*. 2014, vol. 8, pp. 605–609. Available from DOI: 10.1038/nphoton.2014.139.
70. DURDEVIC, L.; ROBERT, H. M. L.; AL., B. Wattellier et. Microscale Temperature Shaping Using Spatial Light Modulation on Gold Nanoparticles. *Sci Rep*. 2019, vol. 9. Available from DOI: 10.1038/s41598-019-40382-3.
71. YEH, P.; GU, C. *Optics of liquid crystal displays*. Wiley-Interscience, 1999. ISBN 9780471182016.
72. SINGH, S.; DUNMUR, D. A. *Liquid crystals fundamentals*. World Scientific Publishing Company, 2002. ISBN 9789810242503.
73. YANG, Deng-Ke; WU, Shin-Tson. *Fundamentals of liquid crystal devices*. John Wiley and Sons, 2014. ISBN 978-1-118-75200-5.
74. PASCHOTTA, R. *Liquid Crystal Modulators* [online]. RP Photonics AG, 2019 [visited on 2023-11-28]. Available from DOI: 10.61835/tve.
75. ZHANG, Z.; YOU, Z.; CHU, D. Fundamentals of phase-only liquid crystal on silicon (LCOS) devices. *Light: Science & Applications*. 2014, vol. 3. Available from DOI: 10.1038/lsa.2014.94.
76. PASCHOTTA, R. 'Deformable mirrors' the *RP Photonics Encyclopedia*. 2023-11-08. Available also from: https://www.rp-photonics.com/deformable_mirrors.html.
77. AKBULUT, D.; HUISMAN, T. J.; PUTTEN, E. G. van; VOS, W. L.; MOSK, A. P. Focusing light through random photonic media by binary amplitude modulation. *Opt. Express*. 2011, vol. 19, pp. 4017–4029. Available from DOI: 10.1364/OE.19.004017.
78. NAM, Kibum; PARK, Jung-Hoon. Increasing the enhancement factor for DMD-based wavefront shaping. *Opt. Lett.* 2020, vol. 45, pp. 3381–3384. Available from DOI: 10.1364/OL.394752.
79. LIANG, M.; STEHR, R. L.; KRAUSE, A. W. Confocal pattern period in multiple-aperture confocal imaging systems with coherent illumination. *Opt. Lett.* 1997, vol. 22, pp. 751–753. Available from DOI: 10.1364/OL.22.000751.
80. FUKANO, T.; MIYAWAKI, A. Whole-field fluorescence microscope with digital micromirror device: imaging of biological samples. *Appl. Opt.* 2003, vol. 42. Available from DOI: 10.1364/AO.42.004119.
81. LIAO, X.; BROWN, K. A.; SCHMUCKER, A. L.; LIU, G.; HE, S. and. Desktop nanofabrication with massively multiplexed beam pen lithography Shim, W. and Mirkin, C. A. *Nature Communications*. 2013, vol. 4. Available from DOI: 10.1038/ncomms3103.
82. AYOUB, A. B.; PSALTIS, D. High speed, complex wavefront shaping using the digital micro-mirror device. *Scientific Reports*. 2021, vol. 11. Available from DOI: 10.1038/s41598-021-98430-w.
83. PASCHOTTA, R. 'Acousto-optic modulators' in the *RP Photonics Encyclopedia*. 2023-11-14. Available also from: https://www.rp-photonics.com/acousto_optic_modulators.html.

84. PASCHOTTA, R. 'Acousto-optic deflectors' in the *RP Photonics Encyclopedia*. 2023-11-14. Available also from: https://www.rp-photonics.com/acousto_optic_deflectors.html.
85. SAVAGE, N. Acousto-optic devices. *Nature Photonics*. 2010, vol. 4. Available from DOI: 10.1038/nphoton.2010.229.
86. TREPTOW, D.; BOLA, R.; MARTÍN-BADOSA, E.; MONTES-USATEGUI, M. Artifact-free holographic light shaping through moving acousto-optic holograms. *Scientific Reports*. 2021, vol. 11. Available from DOI: 10.1038/s41598-021-00332-4.
87. LIU, X.; BRAVERMAN, B.; BOYD, R. W. Using an acousto-optic modulator as a fast spatial light modulator. *Opt. Express*. 2023, vol. 31, pp. 1501–1515. Available from DOI: 10.1364/OE.471910.
88. BRAVERMAN, B.; SKERJANC, A.; SULLIVAN, N.; BOYD, R. W. Fast generation and detection of spatial modes of light using an acousto-optic modulator. *Opt. Express*. 2020, vol. 28, pp. 29112–29121. Available from DOI: 10.1364/OE.404309.
89. OKAMOTO, T.; KAMIYAMA, T.; YAMAGUCHI, I. All-optical spatial light modulator with surface plasmon resonance. *Opt. Lett.* 1993, vol. 18, pp. 1570–1572. Available from DOI: 10.1364/OL.18.001570.
90. ROBERT, H. M. L.; ČIČALA, M.; PILIARIK, M. Shaping of Optical Wavefronts Using Light-Patterned Photothermal Metamaterial. *Advanced Optical Materials*. 2022. Available from DOI: 10.1002/adom.202200960.
91. LIN, Shupeii; HE, Yong; PILIARIK, Marek; CHEN, Xue-Wen. *Optical Fingerprint of Flat Substrate Surface and Marker-free Lateral Displacement Detection with Angstrom-level Precision*. arXiv, 2022. Available from DOI: 10.48550/ARXIV.2208.09772.
92. YONG, H.; SHUPEI, L.; ROBERT, H. M. L.; HONG, L.; PU, Z.; PILIARIK, M.; XUE-WEN, Ch. Multiscale modeling and analysis for high-fidelity interferometric scattering microscopy. *J Phys. D:Appl. Phys.* 2021, vol. 54. Available from DOI: doi:10.1088/1361-6463/abf70d.
93. GOYAL, A.; KUMAR, A.; PATRA, P. K.; MAHENDRA, S.; TABATABAEI, S.; ALVAREZ, P. J. J.; JOHN, G.; AJAYAN, P. M. In situ Synthesis of Metal Nanoparticle Embedded Free Standing Multifunctional PDMS Films. *Macromolecular Rapid Communications*. 2009, vol. 30, pp. 1116–1122. Available from DOI: <https://doi.org/10.1002/marc.200900174>.